



Article

# TU1208 Open Database of Radargrams: The Dataset of the IFSTTAR Geophysical Test Site

Xavier Dérobert <sup>1</sup>  and Lara Pajewski <sup>2,\*</sup> 

<sup>1</sup> Institut Français des Sciences et Technologies des Transports, de l'Aménagement et des Réseaux (IFSTTAR), CS 04–44344 Bouguenais CEDEX, France, xavier.derovert@ifsttar.fr

<sup>2</sup> Department of Information Engineering, Electronics and Telecommunications, Sapienza University of Rome, via Eudossiana 18, 00184 Rome, Italy

\* Correspondence: tu1208@gpradar.eu or lara.pajewski@uniroma1.it; Tel.: +39-06-4458-5358

Received: 16 February 2018; Accepted: 26 March 2018; Published: 29 March 2018



**Abstract:** This paper aims to present a wide dataset of ground penetrating radar (GPR) profiles recorded on a full-size geophysical test site, in Nantes (France). The geophysical test site was conceived to reproduce objects and obstacles commonly met in the urban subsurface, in a completely controlled environment; since the design phase, the site was especially adapted to the context of radar-based techniques. After a detailed description of the test site and its building process, the GPR profiles included in the dataset are presented and commented on. Overall, 67 profiles were recorded along eleven parallel lines crossing the test site in the transverse direction; three pulsed radar systems were used to perform the measurements, manufactured by different producers and equipped with various antennas having central frequencies from 200 MHz to 900 MHz. An archive containing all profiles (raw data) is enclosed to this paper as supplementary material. This dataset is the core part of the Open Database of Radargrams initiative of COST (European Cooperation in Science and Technology) Action TU1208 “Civil engineering applications of Ground Penetrating Radar”. The idea beyond such initiative is to share with the scientific community a selection of interesting and reliable GPR responses, to enable an effective benchmark for direct and inverse electromagnetic approaches, imaging methods and signal processing algorithms. We hope that the dataset presented in this paper will be enriched by the contributions of further users in the future, who will visit the test site and acquire new data with their GPR systems. Moreover, we hope that the dataset will be made alive by researchers who will perform advanced analyses of the profiles, measure the electromagnetic characteristics of the host materials, contribute with synthetic radargrams obtained by modeling the site with electromagnetic simulators, and more in general share results achieved by applying their techniques on the available profiles.

**Keywords:** ground penetrating radar; non-destructive testing; near-surface geophysics; test site

## 1. Introduction

In this paper, a wide collection of ground penetrating radar (GPR) [1,2] profiles is presented. All data were recorded over the Nantes geophysical test site of the French institute of science and technology for transport, spatial planning, development and networks (Institut français des sciences et technologies des transports, de l'aménagement et des réseaux, IFSTTAR).

The Nantes geophysical test site of IFSTTAR has been in service for twenty years. It was conceived to reproduce a scenario including full-size objects and obstacles commonly found in urban grounds, in a completely controlled environment. Since the design phase, the site was especially adapted to the context of radar-based techniques. The main needs for the urban civil engineering, in which this site intends to provide an experimental field, relate to the non-destructive detection, localization

and characterization of hidden structures and not to the assessment of soil properties. The detection of underground structures in urban environments is definitely a crucial problem and geophysical methods, particularly GPR, can perform this task with relatively good efficiency, depending on the physical properties of the host material, the physical and geometrical properties of the sought bodies, and the overall framework. As a tool accessible to professionals, the IFSTTAR test site has been logically used for needs such as tests or comparisons of devices, and validation of measurement or modeling methods.

The test site [3] consists of a pit, 30 m long and 5 m wide, with sloping sides. The useful region of the pit has a variable depth around 4 m. The pit is divided into five sections, filled with different materials such as silt, limestone and gneiss, and separated by vertical interfaces. Several targets are embedded in the test site and accurately geo-referenced. They are representative of objects that can be generally met in trenchless works—such as pipes, cables, stones of various size, and masonry. Precautions were taken to prevent water inflows, to avoid any bias in GPR measurements due to environmental changes. To ensure optimum data acquisition, the site is easily accessible and far from noise sources such as electrical installations and trees.

The dataset subject of this paper includes 67 radargrams recorded by using three commercial pulsed GPR systems equipped with various antennas working on different ranges of the electromagnetic spectrum, and in particular with central frequencies from 200 MHz to 900 MHz. Measurements were performed along 11 parallel lines, crossing the test site in the transverse direction. The dataset is the core part of the Open Database of Radargrams initiative of COST (European Cooperation in Science and Technology) Action TU1208 “Civil engineering applications of Ground Penetrating Radar” [4,5], which consists in realizing and making available an open collection of interesting GPR responses (experimental and synthetic) to enable a very effective benchmark for forward and inverse electromagnetic scattering methods imaging techniques and signal processing algorithms. Actually, numerous studies in the literature present and sometimes compare analytical and/or numerical methods for the analysis and interpretation of GPR data; but, each approach is generally considered individually in a specific context and compared with a limited number of other methods. The availability of a reference set of GPR profiles is a turning point in this field of research, because it facilitates a wider, more effective and rigorous comparison of different techniques. All data of the TU1208 database are being shared with the scientific community via the Action website and/or dedicated open access publications (such as this paper), along with detailed descriptions of the investigated structures and full information about the employed equipment. To the best of our knowledge, TU1208 Open Database of Radargrams is the first open collection of GPR responses: Similar initiatives were never undertaken in the past, in the GPR field.

The paper is structured as follows. In Section 2, COST Action TU1208 is shortly introduced; the objectives of the Open Database of Radargrams are outlined and the context in which the initiative was born is portrayed. In Section 3, the geophysical test site is described in detail: schematic maps and sections of the site, as well as photos shot during the site construction, are presented; moreover, information about the filling materials and buried targets is given. We would like to underline that, although the site was built in 1996, such a comprehensive explanation of its realization method, geometry, and nature of the involved materials, was not published before on the international scientific literature. In Section 4, full information about the GPR equipment used to perform the measurements and relevant data-collection settings is provided. In Section 5, all profiles are plotted in grey-scale maps and several comments are given, which we deem useful for facilitating the comprehension and usage of the data. Conclusions are drawn in Section 6, where plans for future work are traced and ideas for possible investigations based on the presented dataset are suggested.

## 2. COST Action TU1208 and the Open Database of Radargrams Initiative

COST Action TU1208 was running from April 2013 to October 2017 [4,5]. It involved more than 300 experts from 150 partner institutes in 28 COST countries (Austria, Belgium, Croatia, Czech Republic,

Denmark, Estonia, Finland, France, former Yugoslav Republic of Macedonia, Germany, Greece, Ireland, Italy, Latvia, Malta, the Netherlands, Norway, Poland, Portugal, Romania, Serbia, Slovakia, Slovenia, Spain, Sweden, Switzerland, Turkey, and the United Kingdom), a COST cooperating state (Israel), 6 COST near neighboring countries (Albania, Armenia, Egypt, Jordan, Russia, Ukraine) and 6 COST international partner countries (Australia, Colombia, Hong Kong, The Philippines, Rwanda, the United States). University researchers, software developers, civil and electronic engineers, archaeologists, geophysics experts, non-destructive testing equipment designers and manufacturers, end-users from private companies and public agencies participated in the Action.

The primary objective of COST Action TU108 was to exchange and increase scientific-technical knowledge and experience of GPR technique, whilst promoting a wider and more effective use of this safe and non-destructive method. The scientific structure of the Action included four Working Groups (WGs), which research activities covered all areas of GPR technology, methodology, and applications. The Open Database of Radargrams is a joint outcome of WG 2 and WG 3.

WG 1 focused on the development of novel GPR instrumentation. Within this WG, novel equipment was designed, implemented and tested [6–11]. Moreover, new tests were proposed for checking the performance and stability of GPR systems.

WG 2 focused on the use of GPR in civil engineering. This WG developed guidelines for GPR inspection of flexible pavements, utility detection in urban areas, and evaluation of concrete structures (the afore mentioned system performance compliance tests are included in these guidelines, which are currently being refined before being published). Recommendations for a safe use of GPR were produced [12]. A catalogue of available test sites and laboratories, where GPR equipment, methodology and procedures can be tested, was prepared and is available online [13]. Additionally, WG 2 carried out a wide series of case studies where GPR was successfully employed in civil-engineering works and laboratory tests; some examples are found in [14–20].

WG 3 studied electromagnetic forward [21–24] and inverse [25,26] methods for the solution of near-field scattering problems by buried structures, imaging techniques [27–30] and data processing algorithms [31–33]. The Members of this WG contributed to the Action by developing and releasing free software, including a new and open-source version of the well-known finite-difference time-domain (FDTD) simulator gprMax [34] and further tools for GPR modeling and data analysis [35–38].

WG 4 investigated the joint use of GPR and complementary non-destructive testing methods in civil engineering [39–43]. This WG also dealt with the use of GPR outside from the civil engineering area. The most interesting output of this WG is a wide series of real-field case studies showing how GPR can be effectively employed in well-established and emerging applications; some examples are found in [44–47]. Special attention was paid to the use of GPR for the management of cultural heritage [48–52].

All WGs were active in organizing meetings, workshops, conferences, special sessions, a series of dissemination events (GPR Road Show), and training activities (fifteen Training Schools were offered in four years). The Action also produced an open-access educational package for teaching GPR in the university (TU1208 Education Pack, available on the Action website). As a follow-up of COST Action TU1208, a non-profit association was founded in September 2017 (TU1208 GPR Association), to keep the scientific network alive and further support cooperation between Universities, research centers, private companies and public agencies active in the GPR field.

The Open Database of Radargrams project consists in gathering and organizing a collection of interesting GPR profiles, which are made accessible to scientists willing to test and validate, against reliable data, their electromagnetic modeling, inversion, imaging and signal-processing methods. Descriptions of the inspected structures and employed equipment are provided along with the profiles. It is often difficult, for scientists involved in theoretical and numerical studies, to get access to high-quality usable experimental data, and this is one of the reasons why we believe that the Open Database of Radargrams is a promising initiative. By using analytical and numerical techniques for the solution of forward scattering problems, scientists can try and reproduce the data included in the

database, by modeling the scenario at hand. Inversion and imaging methods can be applied to the various radargrams, to try and reconstruct the geometrical and physical properties of the inspected subsurface or structures. The effectiveness of signal processing algorithms and procedures can be verified and tested. An impressive result, which we hope can be achieved by the GPR scientific community in the forthcoming years, will be that of describing the state of the art of the research in the field by applying different techniques to the radargrams included in the database. Let us point out that this open-science initiative does not aim at defining the “best” methods but more properly at indicating the range of reliability and efficiency of each approach in terms of accuracy, potential, advantages, and drawbacks.

The idea to start the database came out during a TU1208 Short-Term Scientific Mission [53]. It was lately discussed during a WG 3 meeting of the Action [54] and presented at the 2015 edition of the European Geosciences Union General Assembly [55]. It takes inspiration by successful past ventures carried out in different areas. For example, the Ipswich database [56–58] in the field of free-space electromagnetic scattering is a collection of experimental X-band data measured on metallic and dielectric scatterers, in anechoic chamber, at the USAF (United States Air Force) Ipswich Measurement Facility. The subsequent Fresnel database [59–62] aims at extending the scope of applications and includes data measured over a wider frequency range, on a series of homogeneous scatterers, in the anechoic chamber of the Centre Commun de Ressources Microondes at Marseille, France. The Marmousi database [63] in seismic science is a two-dimensional synthetic dataset generated at the Institut Français du Pétrole at Rueil-Malmaison Cedex, France. The geometry of the model is inspired by a real profile through the North Quenguela in the Cuanza basin, in Angola; the model was used to create complex data, which require advanced processing techniques to obtain a correct image of the earth. The Marmousi database was used for a workshop on practical aspects of seismic data inversion, during the 52nd EAEG (European Association of Exploration Geophysicists) meeting held in Copenhagen in 1990, and was subsequently studied by hundreds of researchers through the years. The Musumeci database [64], of interest for scientists who analyze seismic events, is a dataset of 151 events leading the 17 July–9 August 2001 lateral eruption at Mt. Etna volcano, in Italy.

As said in the Introduction, the dataset presented in this paper is the core of the Open Database of Radargrams, both because it is the most complete (it includes a high number of profiles, measured with pulsed radar systems produced by three different manufactures and equipped with several antennas working in various frequency ranges) and it was obtained in a controlled environment (complete information concerning the geometry of the test site is available). Another interesting dataset included in the database comes from GPR measurements performed over the historical masonry bridge of Traba, in Spain [65]. Data were recorded by using two commercial pulsed GPR systems, both equipped with 250 MHz and 500 MHz antennas; two-dimensional gprMax models of the bridge and relevant simulation results are available, as well. The database comprises also GPR responses recorded on a masonry column of the Hospital de Sant Pau i la Santa Creu in Barcelona, Spain [40]. The column has a complex internal structure and data were recorded with a commercial pulsed system equipped with an antenna having a central frequency of 1600 MHz. In [53], a series of synthetic profiles was produced by implementing and executing two dimensional gprMax models of concrete cells hosting various metallic reinforcing elements, as well as dielectric and metallic pipes. This dataset was subsequently enriched with several new synthetic profiles, obtained by adopting a more accurate representation of concrete (which takes into account its frequency-dispersion properties); the distance between the targets embedded in concrete and their size were also varied. A further interesting synthetic dataset was obtained by implementing and executing a realistic three-dimensional gprMax model of a fictional but realistic landmine detection environment, with several targets. This dataset was prepared for the GPR Imaging Challenge of the 9th International Workshop on Advanced Ground Penetrating Radar (IWAGPR 2017); researchers attending the conference were invited to submit their processing, imaging and inversion results, to be presented and discussed during the event [66].

### 3. Description of the IFSTTAR Geophysical Test Site

The IFSTTAR geophysical test site was constructed in 1996, in the IFSTTAR Nantes Centre, in France (see Figure 1). The site is located in the northern sector of the research center area, close to the canteen and to the edge of the property. The test site can be used to test, compare and validate various geophysical equipment and methods, including GPR [67]. Further possible uses include training and demonstration activities.

A schematic plan view of the test site is presented in Figure 2, along with a sketch of its longitudinal section; on the plan view, eleven red arrows represent the acquisition lines of GPR profiles. A pit was excavated in the ground, in a region where the soil has a natural slope, which guarantees that the site is easily drainable. The ground support of the pit, visible in the photo reported in Figure 3a, consists of very altered mica schists, with an almost vertical dip and a cleavage perpendicular to the slope, certainly very absorbent to electromagnetic waves. The photo in Figure 3b shows that the pit was dug with the longitudinal axis parallel to the direction of the land slope, to facilitate the evacuation of water. The excavation background is 5 m wide, with a slope of 4%; the pit is 30 m long and its useful region has a variable depth, ranging from 3.30 m to 4.70 m. The pit sides have a slope of 2/1, which means that the pit surface width is between 19 m and 24.60 m, the surface slope being reduced to 1%. The materials filling the five transversal trenches of the site are described in Section 3.1. To avoid any water ingress, whatever incoming (rain, water flow, capillary ingress), the test site is protected with different elements described in detail in Section 3.2. The targets embedded in the site are described in Section 3.3. Finally, Section 3.4 is concerned with the methods employed to geo-locate the site targets.

For interested users, several photos and videos of the construction phases are available on request, as well as a complete topographical file describing the geometry of the pit, the position of each buried object, and the topography of the finished surface. Moreover, photos of each buried object and details of its composition are available, too, and samples of each type of soil.

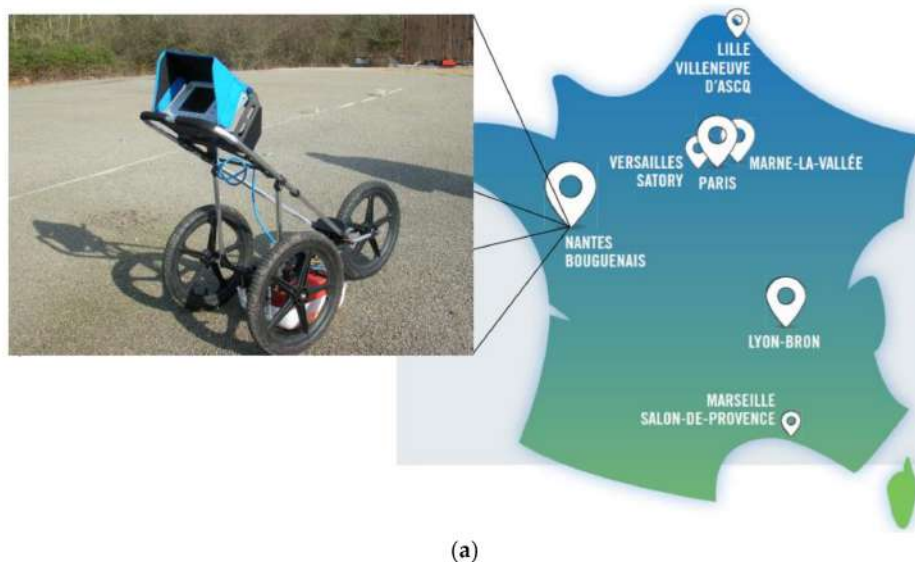
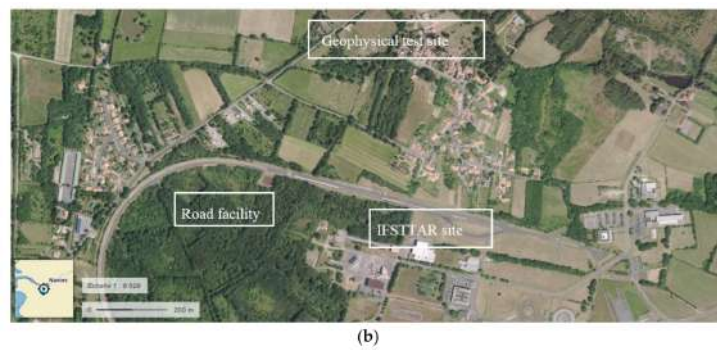
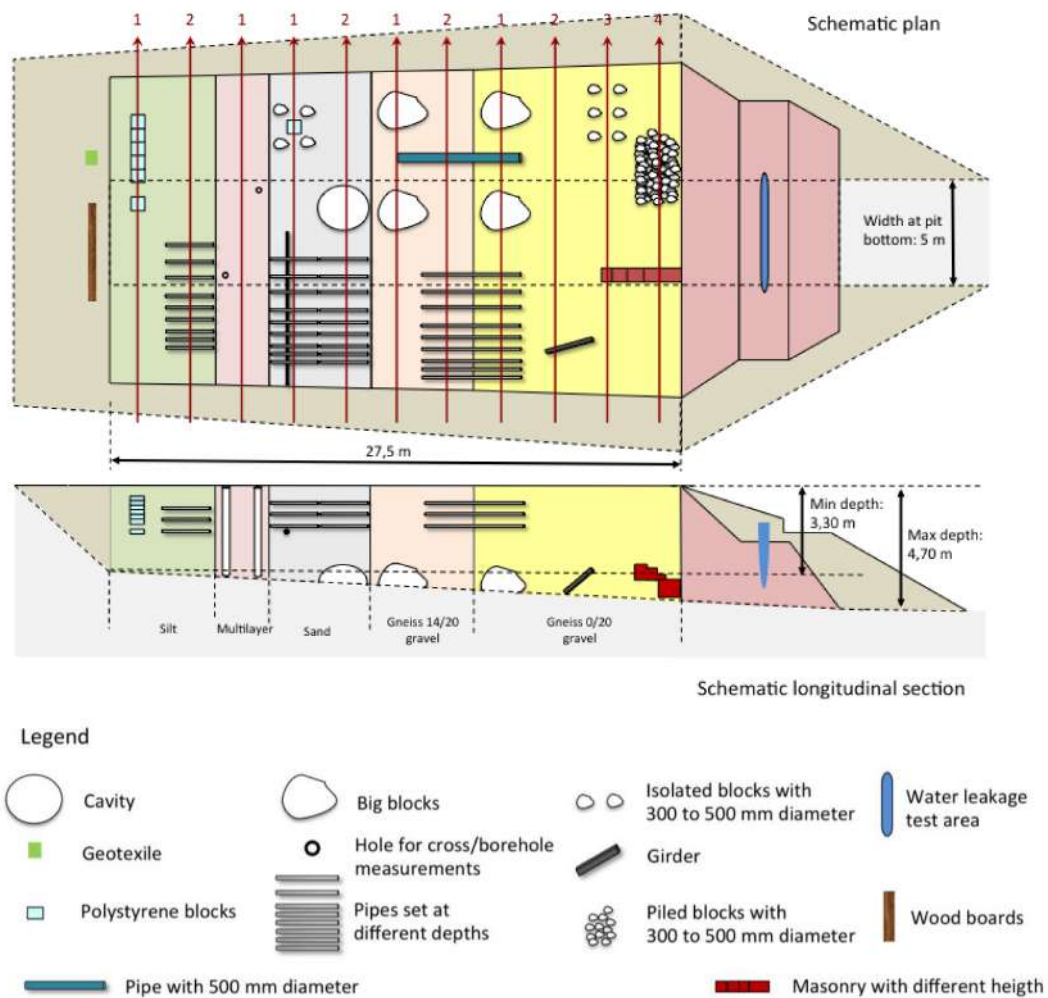


Figure 1. Cont.





**Figure 1.** Geographical position of the IFSTTAR geophysical test site. (a) Map of France, where the test site location is indicated; (b) Aerial photo (taken from the website of the French Ministry ‘Ministère français de la Transition Écologique et Solidaire’, [www.geoportail.gouv.fr/carte](http://www.geoportail.gouv.fr/carte)) showing the test site area.



**Figure 2.** Schematic plan view of the test site and longitudinal section. Red arrows represent the acquisition lines of GPR profiles.



**Figure 3.** (a) Excavation of the mica schist ground support; (b) shape of the test site between embankments.

### 3.1. Filling Materials

The pit is divided into five transversal trenches, corresponding to eleven 2.5-m long sections (transverse slices) for GPR surveys, filled with different materials and separated by vertical interfaces. In particular, there are (Figure 2):

- Two adjacent sections filled with silt (hence, the silt region is 5 m long, altogether);
- A multilayered section, consisting of a stack of layers of different materials which thicknesses from 0.60 m to 1.30 m;
- Two adjacent sections of limestone (hence, the limestone region is 5 m long);
- Two sections filled with Gneiss 14/20 gravel (therefore, the overall length of the low-density gravel region is 5 m; the density is approximately  $1.8 \text{ t/m}^3$ ); and
- Four sections filled with Gneiss 0/20 gravel (all in, the high-density gravel region is therefore 10 m long; and the density is around  $2.2 \text{ t/m}^3$ ).

Gneiss 14/20 and Gneiss 0/20 are crushed gneiss with a grain size from 14 mm to 20 mm, and from 0.1 mm to 20 mm, respectively. Above all sections, a layer of washed 0/2 sand was placed, having a thickness of 10 cm. In each region, it is possible to find places without any buried target, in order to calibrate measurements either over the lateral slope or over the pit bottom. The various filling materials were chosen to be representative of urban environments (e.g., presence of silt, limestone basins), while being relatively “pure”, thus allowing a reasonably easy numerical modeling of the test site. The sloping sides were mainly realized with excavated materials.

Materials are characterized by their density, rate of fines, the Methylene Blue Value (MBV, which globally expresses the quantity of clay contained in a material), the maximum diameter of the aggregates and the optimal Proctor value (conceived to determine the optimal moisture content at which a given soil becomes most dense and achieves its maximum dry density). For practical reasons, the MBV value, which follows a French standard, is correlated with two international values [68]: The Cation Exchange Capacity (CEC), which quantifies how many cations can be retained on soil particle surfaces, and the activity  $A_c$ , defined by Skempton [69] as the ratio of the plasticity index of clay  $I_p$  to its content of clay particles (noted  $C_2$ , content of particles smaller than  $2 \mu\text{m}$ ). The physical properties of the test site filling materials are resumed in Table 1.

The silt comes from a construction site at “Le Loup du Lac”, along the National Route No. RN12 connecting Rennes and St Brieuc, in the Ille-et-Vilaine department of France that is located in the region of Brittany, in the northwest of the country; the classification of the silt in the G.T.R. 92 French standard is A1. The calcareous (limestone) sand comes from an area close to Arthon, about 15 km from Nantes, next to the south bank of the Loire, where a deposit of consolidated (but very friable) sand is present, dated from the Tertiary and more specifically from the Lutetian; the G.T.R. 92 classification is R4; the humidity level in the sand sections of the test site was controlled during the construction of the test site and it was approximately equal to the optimal Proctor value. The Gneiss gravel comes from Chassé,

a French village located in the Sarthe department, in the region of the Pays de la Loire. The sand used for a 10-cm layer covering the entire test site comes from a quarry along the “Carrière de Petit Mars” road going from Chasse to Chemin des Masses, close to St Mars du Désert, about 20 km north of Nantes; the aggregate range is 0–5mm, with 15% of fines.

**Table 1.** Physical characteristics of the filling materials.

Physical Characteristic	Silt	Limestone	Gneiss 14/20	Gneiss 0/20
Dry density (t/m <sup>3</sup> )	-	1.74–1.90	1.8–1.9	2.2
Fines < 80 mm (%)	98	13–19	-	< 1
D max aggr. (mm)	≤2	0.8–2	20	20
MBV	0.73–2	0.16–0.56	-	-
CEC (cmol <sup>+</sup> /kg)	3.11–7.50	1.15–2.53	-	-
Ac = Ip/C <sub>2</sub> (mm)	0.35–0.42	0.32–0.34	-	-
Optimum water content (Proctor Opt. %)	10	12–15	-	-

In order to obtain a good compaction, the pit was filled in small layers (slices), having a thickness of 20 cm; beginning at the pit far end, each slice was filled while being separated from the following one by a wood board. A first compaction was performed with hand driven mechanical tools, on each side of the board and all around the buried objects; boards were then pulled out and a 13 T compactor was used over the total layer (Figure 3). The main difficulties were due to: the differences in behavior of the various soils under compaction, so that the limits between the slices tended to bend (due to this, one should consider that the vertical interfaces between different region are not abrupt and planar, and that a melted region about 0.50 m wide is present); the compaction near the lateral slope was more difficult because of the presence of the geosynthetic drain.

### 3.2. Protection against Water

The protection against water is a key issue in the realization of a test site, where controlled and known conditions are sought, to guarantee reproducibility of the results. A possible solution for making a site completely waterproof is to place a geomembrane below it and a tarp above; else, a building can be constructed, to contain and protect the whole test site. However, a waterproof geomembrane is very expensive, especially in a rocky region as the one where the IFSTTAR geophysical test site is realized. As for the construction of a building, this is obviously even more expensive. Those optimal solutions were excluded when the IFSTTAR geophysical test site was designed, due to financial constraints; several alternatives were considered and studied, and finally, it was decided to realize an underground structure against water inflow and a surface structure against rain and snow, as described in the following.

The underground structure of protection against water was realized before filling the pit and consists of:

- A Gneiss 14/20 gravel layer, 20 cm thick, coated above and below by a geotextile. This drainage layer is present throughout the entire bottom of the pit and it is open at the end of its lowest side; it collects water from the surrounding soil. In the drainage layer, two PVC tubes with a 10 cm diameter are present, which can serve to pass drill-type probes (see Figure 4a).
- A Gneiss 14/20 gravel mask at the beginning of the pit, before the silt region, to protect the site against surrounding subsoil water and to achieve a vertical limit of the silt region.
- A three-layer geotextile for the drainage of the sides of the entire site, composed by: A layer of geotextile (BIDIM 300, which is a standard anti-contaminant layer), a plastic grid made of two crossed wire networks (Tenax grid) to ensure water transmissivity, and another layer of geotextile (BIDIM 300) to ensure permeability. This multilayer drives directly water from the lateral embankments to the bottom drain (see Figure 4b).



The surface protection against rain and snow is achieved by means of:

- A coating layer, realized by spreading a bituminous emulsion with 69% density (having a weight of  $1.5 \text{ kg/m}^2$ ), by lying over it a geotextile with  $200 \text{ g/m}^2$  weight, and by finally spreading again a bituminous emulsion with 69% density (having a weight of  $2.5 \text{ kg/m}^2$ ). Some Gneiss 2/4 gravels were embedded in the upper bituminous emulsion of the coating layer, for circulation and protection from the sun (Figure 5).
- Side trenches, located outside the test site platform, at the foot of the embankments.
- An asphalt flange at the downstream end of the site, to evacuate laterally the water that would otherwise trickle longitudinally and erode the slope.



Figure 4. (a) Bottom and; (b) lateral watertight during the placement.



Figure 5. Placement of the 3-layer asphalt wearing.

### 3.3. Targets

Several targets are present in the test site; they are representative of objects that can be commonly found in trenchless works—such as pipes, cables, stones of various sizes, masonry, and more. Table 2 offers an overview on target types, possible objectives of non-destructive investigations in their presence, and general information about targets actually embedded in the test site. In the following of this sub-section, more detailed information is provided for all the test site targets.

**Table 2.** Target types, possible objectives of a non-destructive investigation, general properties of the targets embedded in the test-site.

Targets	Aims of a Non-Destructive Investigation	General Information about Targets in the Test Site
Pipes	Detecting the presence of pipes and tracking their location in plan and depth. Identifying pipe crossings, which may cause perturbation. Detecting and tracking particularly large pipes.	Groups of 3 pipes at the same depth; 3 different depths; 4 different enclosing materials. One area with electric cables crossing the pipes. Presence of pipes with $\text{Ø}500$ .
Voids	Detecting the presence of voids and evaluating their depth.	Staircase of $1 \text{ m}^2$ polystyrene blocks, simulating voids, in the section filled with the most absorbing material for the electromagnetic waves (silt).

Table 2. Cont.

Targets	Aims of a Non-Destructive Investigation	General Information about Targets in the Test Site
Laminate soils	Estimation of thicknesses and material properties.	Multilayered section with holes for crosshole/borehole/tomography measurements.
Rocky blocks	Detecting the presence of rocky blocks, estimating their position and differentiating them according to their size.	Blocks with 3 different sizes (Ø300 mm, Ø500 mm, and 4 m <sup>3</sup> ), in different host materials. The Ø300 mm and Ø500 mm stones are at 3 different depths; the 4 m <sup>3</sup> blocks are at 2 different depths.
Reproducibility of results—host materials with different density	Checking the GPR performance in the presence of host materials with different density.	Gravel with expected density of 1.8 and 2.2.
Masonry	Detection and localization.	Masonry blocks at different depths.
Metallic objects	Detection, localization, shape estimation.	Girder obliquely buried.

### 3.3.1. Silt Region

The transversal section of the silt region is schematized in Figure 6. It has to be mentioned that the top of this section was finalized with about 30 cm of limestone (material from the third region), due to lack of silty material; such layer is not represented on the scheme. Moreover, all transversal schemes of the geophysical test site presented in this Section do not show neither the 10-cm surface layer made in limestone nor the asphalt wearing course.

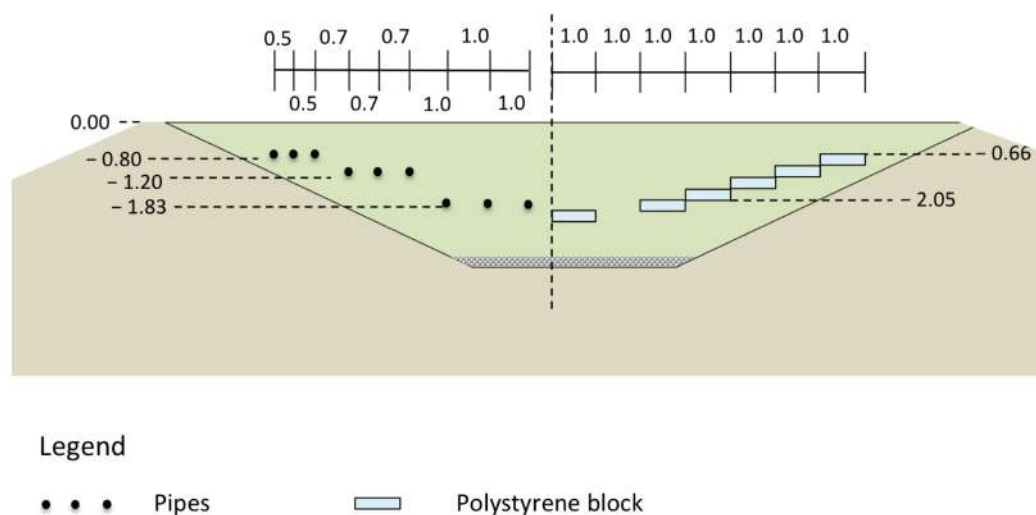


Figure 6. Transversal section of the silt region, showing the embedded targets and their positions. All distances are expressed in meters.

Three pipe layers are present in the silt region, with three pipes per layer: an empty steel pipe, a PVC pipe full of water, and an empty PVC pipe (this is the laying order in all layers, starting from the longitudinal axis of the test site). All pipes are 2.5 m long; the layers are buried at three different depths; the distance between pipes pertaining to the same layer increases with depth. A staircase composed by six expanded polystyrene blocks is also present; the size of the blocks is 1.00 m × 1.00 m × 0.25 m (see the photo in Figure 7).



**Figure 7.** Placement of one of the polystyrene blocks in the silt section.

### 3.3.2. Multilayer Region

A scheme of the transversal section of the multilayer region is presented in Figure 8. There are five layers and no targets. Two vertical holes allow carrying out borehole, crosshole and tomography investigations in this region of the test site.

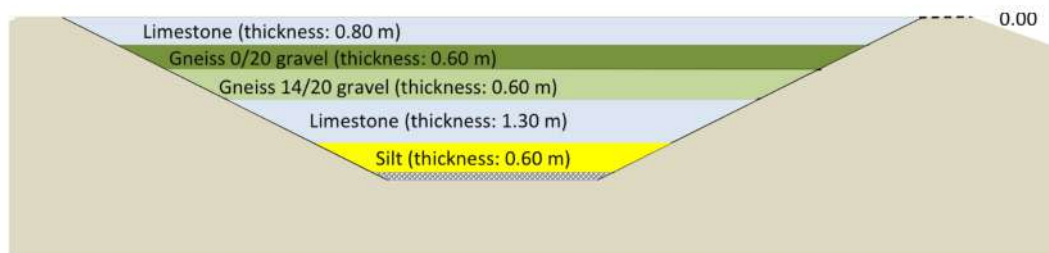


**Figure 8.** Transversal section of the multilayer region, showing the stratification of materials and the thicknesses of the layers.

### 3.3.3. Limestone Region

A scheme of the limestone region is presented in Figure 9 (see also Figure 2, for a better understanding of the description).

Here, two series of pipe layers are present, with the same properties as those embedded in the silt region (Figure 10). This permits performing measurements on the same targets, embedded in different host materials. Moreover, in the first series of pipe layers, a large-section electrical cable per pipe layer is present: The cable is orthogonal to the pipe axes, forms a loop, and is taken out at the edge of the site, in order to optionally be able to feed it. The following objects are also present:

- A hemispherical cavity of expanded polystyrene, with a height of 0.50 m and a diameter of 2.50 m;
- Two couples of isolated gneiss blocks, with 300-mm and 500-mm diameters, buried at two different depths; and
- An expanded polystyrene block with size 1.00 m × 1.00 m × 0.25 m.

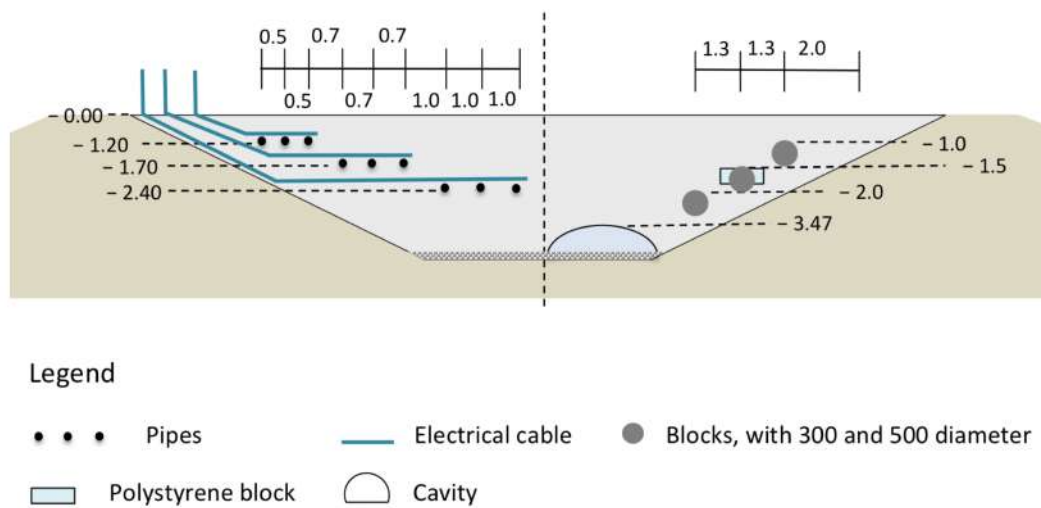


**Figure 9.** Transversal section of the limestone region, showing the embedded targets and their positions. All distances are expressed in meters.



**Figure 10.** Placement of one of the pipe series in the limestone section.

### 3.3.4. Gneiss 14/20 Gravel Region

In this region, the following targets are present (see Figures 11 and 12):

- Three layers of 2.50-m long pipes, same as those described above;
- Two dolmens of about 4 m<sup>3</sup>, consisting of 3 or 4 basic blocks and a capstone, located at different depths; and
- A concrete empty pipe, 2-m long, with a diameter of 500 mm (its ends were sealed with polystyrene plates).



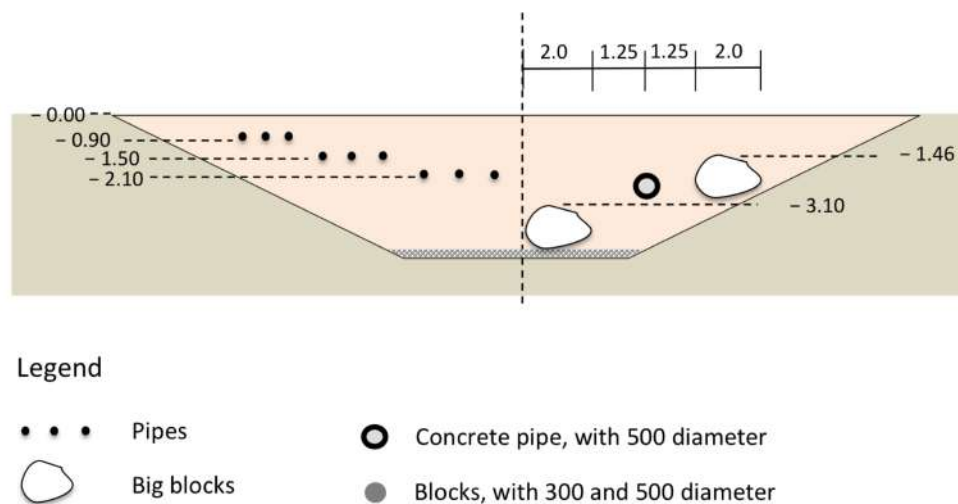


**Figure 11.** Transversal section of the Gneiss 14/20 gravel region, showing the embedded targets and their positions. All distances are expressed in meters.



**Figure 12.** Placement of (a) one of the pipe series in the gneiss sections, and (b) the 500-mm concrete pipe.

### 3.3.5. Gneiss 0/20 Gravel Region

Schemes of the gneiss region are presented in Figure 13 (see also Figure 2, for a better comprehension, and photos in Figure 14). This region is the widest and occupies four modules of the test site. The following targets are present:

- Two dolmens of about 4 m<sup>3</sup>, consisting of three or four basic blocks and a capstone, at different depths;
- a concrete empty pipe, 2-m long, with a diameter of 500 mm (its ends were sealed with polystyrene plates)—this pipe is shared with the Gneiss 0/20 gravel region;
- three layers of 2.50-m long pipes, identical to those previously described;
- a masonry wall of parallelepiped hollow blocks;
- another masonry wall of parallelepiped hollow blocks, with three steps and a total height of about 65 cm;
- a steel girder, obliquely buried and crossing the projection of the acquisition line 2 (the girder is not drawn in Figure 13, because it is ‘hidden’ by the masonry walls);
- a heap of rocky blocks, with diameters from 300 mm to 500 mm, and six isolated blocks, of the same origin as the surrounding Gneiss gravel.

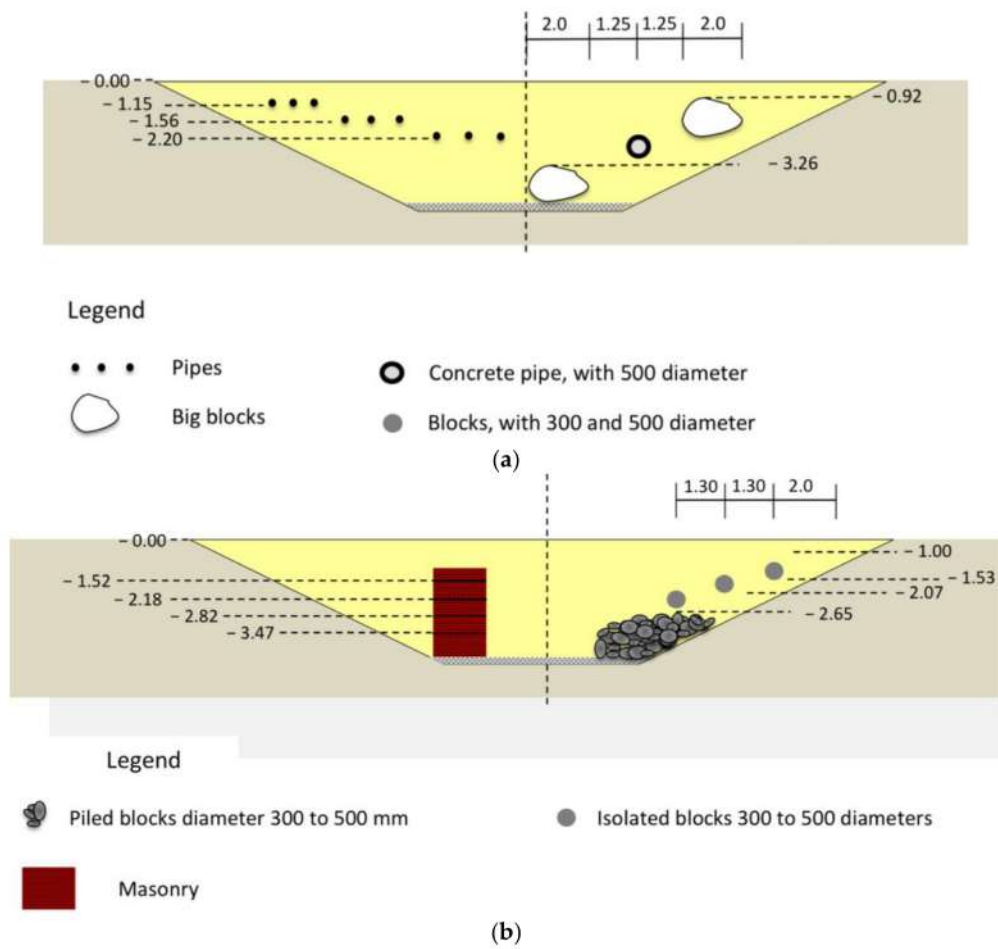


**Figure 13.** Transversal sections of the Gneiss 0/20 gravel region: (a) First part; (b) second part. The embedded objects and their positions are shown. All distances are expressed in meters.

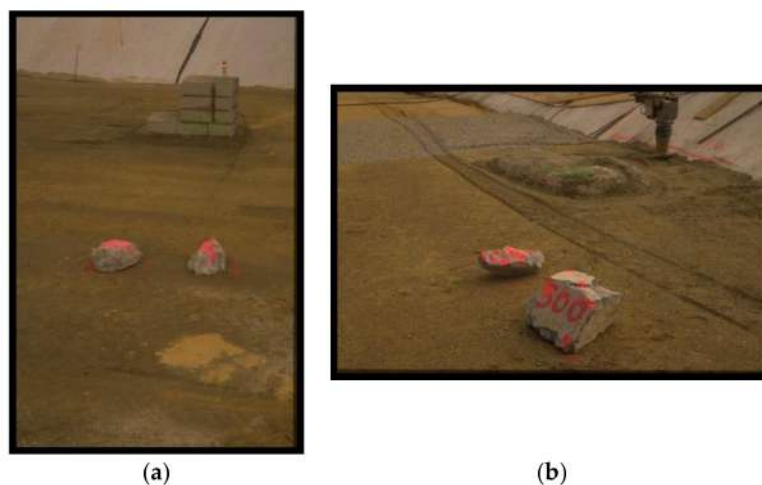


**Figure 14.** Placement of: (a) Isolated blocks and a masonry wall; (b) a heap of rocky blocks.

### 3.4. Geolocation of Targets

During the realization of the test site, every embedded object was carefully geolocated, by using a theodolite (visible in Figure 7). Therefore, each target is positioned from several points: 2 points on the upper side of the pipes at their beginnings and ends, 4 points at the upper angles of the polystyrene blocks, and from 3 to 20 points for the rock blocks and dolmens. The surface of the site was georeferenced on the longitudinal axis and on the sides, for every limit of the sections. For each half-section, an interpolation was performed from the 4 surface angles to obtain the height values above the various targets, and then calculate their respective depths (noted in Figures 6, 8, 9, 11 and 13).

## 4. Equipment and Data Acquisition

Three different GPR systems were used to collect data over the test site, manufactured by GSSI (Geophysical Survey Systems, Inc; Nashua, NH, USA), MALÅ Geoscience (Malå, Sweden), and IDS (Ingegneria dei Sistemi; Pisa, Italy). They were equipped with various antennas, with central frequencies from 200 MHz to 900 MHz. From now on, we will denominate 'GPR 1' the GSSI system, 'GPR 2' the MALÅ system, and 'GPR 3' the IDS system.

GPR 1 was used in bistatic configuration. For measurements performed with 'old' 200-MHz, 400-MHz, 500-MHz, and 900-MHz shielded antennas, the trace spacing was different from one series to another; in some cases, information about the profile length is not available and has to be deducted by analyzing the data. These measurements were performed with antennas manufactured before the Federal Communications Commission (FCC) restrictions on ultra-wideband GPR were emitted. Recently, new measurements were performed by using 200-MHz, 270-MHz, 350 MHz HS (HS stands for hyperstacking), 400-MHz, and 900-MHz last-generation antennas.

For GPR 2, the configuration was bistatic. The distance between the transmitting and receiving antennas was 36 cm with the 250 MHz shielded antenna, 18 cm with the 500 MHz shielded antenna, and 14 cm with the 800 MHz shielded antenna.

With GPR 3, bistatic 200-MHz, 600-MHz, and 900-MHz shielded antennas were tested. Although those antennas were designed before the establishment of the FCC regulation restrictions, they were found suitable for the FCC emission mask. The distance between transmitting and receiving antennas is considered confidential information by the manufacturer, therefore it cannot be provided here.

Data were collected along the eleven red lines shown in Figure 2, as resumed in Tables 3–7; overall, 67 profiles are available. The reason why not all GPR systems and antennas were systematically used over each acquisition line, is that this collection of profiles includes data gathered during different experimental campaigns, carried out by different research teams and for different purposes. Not all the research teams were interested in inspecting all the test site regions.

The file nomenclature is: Freq\_Section\_Optional1Position\_Optional2.ext, where:

- *Freq*: nominal central frequency;
- *Section*: name identifying the section;
- *Position*: number identifying the acquisition line, which can be 1 (profile recorded 1.25 m from the upstream border of the section—left in Figure 2)/2 (3.75 m)/3 (6.25 m)/4 (8.75 m);
- *Optional1*: "h" letter is added just before the position, when a half-length profile is performed (e.g., h1);
- *Optional2*: "rev" when the profile is done in reverse;
- *ext*: file extension, manufacturer dependent.

For data recorded with GPR 1 and the last-generation 200-MHz, 400-MHz, and 900-MHz antennas, a *b* is added before the extension, to distinguish them from data collected with older antennas working at the same frequencies.

In the silt region (Table 3), 15 profiles were recorded by using all GPR systems, with antennas operating at seven different central frequencies. Note that measurements performed over lines 1 and 2 by using GPR 1 with the 200-MHz antenna are (exceptionally) saved in the same file (200MHz\_Silt\_h2h1.dzt) instead of being saved in two separate files. In particular, data were collected on the second half of line 2, over the pipes; then, the acquisition continued on the first half of line 1, over the polystyrene blocks; a discontinuity in the data allows understanding where line 2 data end and line 1 data start.

In the multilayer (Table 4), 4 profiles were recorded, by using GPR 1 and GPR 2 and four different central frequencies.

In the limestone region (Table 5), 15 profiles were recorded, by using all GPR systems and nine different central frequencies.

In the Gneiss 14/20 gravel region (Table 6), 15 profiles were recorded, by using all GPR systems and eight different central frequencies.

Finally, in the Gneiss 0/20 gravel region (Table 7), 18 profiles were recorded by using all GPR systems and eight different central frequencies.

Information about the acquisition settings is given in Tables 3–7, for all regions and data; moreover, information on the settings can of course be found in the data file headers. The profiles from 1999–2000 acquired with GPR 1 system were stored after being pre-processed, by using the settings listed in the tables (the used frequency-band filters were Infinite Impulse Response (IIR)); all other data are available in raw format, without application of any filter nor temporal gain. Concerning the 2017 data acquired with GPR 1, two files are available: a .dzt file, which contains raw data; and a .dzt file, which can be opened by using commercial software developed by the radar manufacturer, where pre-processed data are stored, along with pre-filtering information encoded by the operator on the field (in order to see a better image of the radargram on the screen).



**Table 3.** Information about data collected in the silt region. NA means not available.

Line	GPR System	Year	Antenna Freq (MHz)	File Name	Number of Traces (Profile Length [m])	Scan/m	Sampl./Bits	Range (ns)	Gain (db)	LP (MHz)	HP (MHz)
1	GPR 1	1999	200	200MHz_Silt_h2h1.dzt	1223 (24.44)	50	512/8	110	3/45/70	400	50
		1999	400	400MHz_Silt_1_rev.dzt	1321 (20.02)	66	512/16	70	$-1.202 \times 10^{-6}$	800	100
		1999	500	500MHz_Silt_1_rev.dzt	1324 (NA)	-	512/16	70	$-1.203 \times 10^{-6}$	1000	125
		1999	900	900MHz_Silt_1_rev.dzt	1750 (NA)	-	512/16	60	5/30/50/56/56	1800	225
	GPR 2	2002	250	250MHz_Silt_1_rev.rd3	657 (19.90)	33	413/16	80	-	-	-
		2002	500	500MHz_Silt_1_rev.rd3	1313 (25.80)	50	499/16	89	-	-	-
		2002	800	800MHz_Silt_1_rev.rd3	784 (24.20)	32	721/16	89	-	-	-
	GPR 3	2005	200	200MHz_Silt_h1_rev.dt	486 (9.70)	50	1024/16	100	-	-	-
		2005	600	600MHz_Silt_h1_rev.dt	477 (9.52)	50	1024/16	100	-	-	-
		2005	900	900MHz_Silt_h1_rev.dt	475 (9.48)	50	1024/16	100	-	-	-
2	GPR 1	1999	200	200MHz_Silt_h2h1.dzt	1223 (24.44)	50	512/8	110	3/45/70	400	50
		1999	400	400MHz_Silt_2_rev.dzt	1316 (19.94)	66	512/16	70	$-1.202 \times 10^{-6}$	800	100
		1999	900	900MHz_Silt_2_rev.dzt	1533 (NA)	-	512/16	60	5/30/50/56/56	1800	225
	GPR 3	2005	200	200MHz_Silt_h2_rev.dt	497 (9.92)	50	1024/16	100	-	-	-
		2005	600	600MHz_Silt_h2_rev.dt	474 (9.46)	50	1024/16	100	-	-	-
		2005	900	900MHz_Silt_h2_rev.dt	487 (9.72)	50	1024/16	100	-	-	-

**Table 4.** Information about data collected in the multilayer. NA means not available.

Line	GPR System	Year	Antenna Freq (MHz)	File Name	Number of Traces (Profile Length [m])	Scan/m	Sampl./Bits	Range (ns)	Gain (db)	LP (MHz)	HP (MHz)
1	GPR 1	1999	400	400MHz_ML.dzt	1198 (NA)	-	512/16	70	$-1.202 \times 10^{-6}$	800	100
		1999	900	900MHz_ML.dzt	1777 (NA)	-	512/16	60	5/30/50/56/56	1800	225
	GPR.2	2002	250	250MHz_ML.rd3	733 (22.20)	33	415/16	116	-	-	-
		2002	500	500MHz_ML.rd3	1297 (25.50)	50	499/16	89	-	-	-

**Table 5.** Information about data collected in the limestone region. NA means not available.

Line	GPR System	Year	Antenna Freq (MHz)	File Name	Number of Traces (Profile Length [m])	Scan/m	Sampl./Bits	Range (ns)	Gain (db)	LP (MHz)	HP (MHz)	Stack.	Raw Data (Y/N)	
1	GPR 1	1999	400	400MHz_Limestone_1_rev.dzt	1360 (NA)	-	512/16	85	$-4.547 \times 10^{-7}$	800	100	5	N	
		1999	900	900MHz_Limestone_1_rev.dzt	1757 (NA)	-	512/16	60	5/30/50/56/56	1800	225	5	N	
2	GPR 1	1999	200	200MHz_Limestone_2.dzt	1235 (24.68)	50	512/16	110	3/45/70	400	50	3	N	
		2017	270	270MHz_Limestone_h2.dzt	2571 (12.85)	200	1024/32	100	$-7.639 \times 10^{-5}$	700	75	1	Y	
		2017	350	350MHz_Limestone_h2.dzt	2763 (13.81)	200	512/32	100	$-9.221 \times 10^{-5}$	1095	95	1	Y	
		1999	400	400MHz_Limestone_2_rev.dzt	1418 (NA)	-	512/16	85	$-4.547 \times 10^{-7}$	800	100	5	N	
		2017	400	400MHz_Limestone_h2_b.dzt	2581 (12.90)	200	1024/32	100	$-8.146 \times 10^{-5}$	800	100	1	Y	
		1999	900	900MHz_Limestone2_rev.dzt	1861 (NA)	-	512/16	60	5/30/50/56/56	1800	225	5	N	
		2017	900	900MHz_Limestone_h2_b.dzt	2274 (11.36)	200	1024/32	100	10/37/44/51	-	-	-	1	Y
		GPR 2	2002	250	250MHz_Limestone2_rev.rd3	715 (21.66)	33	415/16	116	-	-	-	1	Y
			2002	500	500MHz_Limestone2_rev.rd3	1172 (23.03)	50	499/16	89	-	-	-	1	Y
			2002	800	800MHz_Limestone2_rev.rd3	825 (25.47)	33	721/16	89	-	-	-	1	Y
GPR 3	2005	200	200MHz_Limestone_2_rev.dt	1053 (21.04)	50	1024/16	100	-	-	-	1	Y		
	2005	600	600MHz_Limestone_2_rev.dt	1038 (20.74)	50	1024/16	100	-	-	-	1	Y		
	2005	900	900MHz_Limestone_2_rev.dt	1042 (20.82)	50	1024/16	100	-	-	-	1	Y		

**Table 6.** Information about data collected in the Gneiss 14/20 gravel region. NA means not available.

Line	GPR System	Year	Antenna Freq (MHz)	File Name	Number of Traces (Profile Length [m])	Scan/m	Sampl./Bits	Range (ns)	Gain (db)	LP (MHz)	HP (MHz)	Stack.	Raw Data (Y/N)
1	GPR 1	1999	400	400MHz_Gneiss14-20_1_rev.dzt	1401 (NA)	-	512/16	70	$-1.202 \times 10^{-6}$	800	100	5	N
		1999	900	900MHz_Gneiss14-20_1_rev.dzt	1473 (NA)	-	512/16	60	5/30/50/56/56	1800	225	5	N
	GPR 2	2002	500	500MHz_Gneiss14-20_1_rev.rd3	1272 (25.00)	50	499/16	89	-	-	-	1	Y
2	GPR 1	1999	200	200MHz_Gneiss14-20_2_rev.dzt	1291 (25.80)	50	512/8	110	3/45/70	400	50	3	N
		2017	200	200MHz_Gneiss14-20_2_b.dzt	4922 (24.60)	200	1024/32	100	7/60/68	1000	100	1	Y
		2017	270	270MHz_Gneiss14-20_2.dzt	4775 (23.87)	200	1024/32	100	-0.0001077	540	50	1	Y
		2017	350	350MHz_Gneiss14-20_2.dzt	5168 (25.83)	200	1024/32	100	$-5.495 \times 10^{-5}$	940	100	1	Y
		2000	400	400MHz_Gneiss14-20_2_rev.dzt	639 (21.27)	30	512/16	90	5/62	665	110	2	N
		2017	400	400MHz_Gneiss14-20_2_b.dzt	2462 (24.61)	100	1024/16	100	0/42/61	800	80	1	Y
		2017	500	500MHz_Gneiss14-20_2.dzt	4838 (24.18)	200	1024/16	100	2/40/56/60	1000	100	1	Y
		1999	900	900MHz_Gneiss14-20_2_rev.dzt	1518 (NA)	-	512/16	60	5/30/50/56/56	1800	225	5	N
		2017	900	900MHz_Gneiss14-20_2_b.dzt	4952 (24.75)	200	1024/16	90	4/11/55/60/62	1800	200	1	Y
		GPR 2	2002	250	250MHz_Gneiss14-20_2_rev.rd3	737 (22.32)	33	415/16	116	-	-	-	1
2002	500		500MHz_Gneiss14-20_2_rev.rd3	1287 (25.29)	50	499/16	89	-	-	-	1	Y	
2002	800		800MHz_Gneiss14-20_2_rev.rd3	820 (25.31)	33	721/16	89	-	-	-	1	Y	

**Table 7.** Information about data collected in the Gneiss 0/20 gravel region. NA means not available.

Line	GPR System	Year	Antenna Freq (MHz)	File Name	Number of Traces (Profile Length [m])	Scan/m	Sampl./Bits	Range (ns)	Gain (db)	LP (MHz)	HP (MHz)	Stack.	Raw Data (Y/N)
1	GPR 1	2017	270	270MHz_Gneiss0-20_h1.dzt	2551 (12.75)	200	1024/32	100	$-7.639 \times 10^{-5}$	700	75	1	Y
		2017	350	350MHz_Gneiss0-20_h1.dzt	2286 (11.42)	200	512/32	100	$-9.221 \times 10^{-5}$	1095	95	1	Y
		2017	400	400MHz_Gneiss0-20_h1.dzt	2490 (12.44)	200	1024/32	100	$-8.146 \times 10^{-5}$	800	100	1	Y
		1999	400	400MHz_Gneiss0-20_1_rev.dzt	1310 (NA)	-	512/16	70	$-1.202 \times 10^{-6}$	800	100	5	N
		2017	900	900MHz_Gneiss0-20_h1.dzt	2409 (12.04)	200	1024/32	100	4/10/37/44/51	-	-	1	Y
		1999	900	900MHz_Gneiss0-20_1_rev.dzt	1837 (NA)	-	512/16	60	5/30/50/56/56	1800	225	5	N
	GPR 2	2002	250	250MHz_Gneiss0-20_1_rev.rd3	754 (22.84)	33	415/16	116	-	-	-	1	Y
		2002	500	500MHz_Gneiss0-20_1_rev.rd3	1234 (24.25)	50	499/16	89	-	-	-	1	Y
		2002	800	800MHz_Gneiss0-20_1_rev.rd3	801 (24.73)	33	721/16	89	-	-	-	1	Y
		2005	200	200MHz_Gneiss0-20_1_rev.dt	1080 (21.58)	50	1024/16	100	-	-	-	1	Y
	GPR 3	2005	600	600MHz_Gneiss0-20_1_rev.dt	1079 (21.56)	50	1024/16	110	-	-	-	1	Y
		2005	900	900MHz_Gneiss0-20_1_rev.dt	1081 (21.60)	50	1024/16	110	-	-	-	1	Y
2	GPR 1	1999	400	400MHz_Gneiss0-20_2_rev.dzt	1860 (NA)	-	512/16	70	$-1.202 \times 10^{-6}$	800	100	5	N
		1999	900	900MHz_Gneiss0-20_2_rev.dzt	1458 (NA)	-	512/16	60	5/30/50/56/56	1800	225	5	N
3	GPR 1	1999	400	400MHz_Gneiss0-20_3_rev.dzt	1447 (NA)	-	512/16	70	$-1.202 \times 10^{-6}$	800	100	5	N
		1999	900	900MHz_Gneiss0-20_3_rev.dzt	1841 (NA)	-	512/16	60	5/30/50/56/56	1800	225	5	N
4	GPR 1	1999	400	400MHz_Gneiss0-20_4_rev.dzt	1672 (NA)	-	512/16	70	$-1.202 \times 10^{-6}$	800	100	5	N
		1999	900	900MHz_Gneiss0-20_4_rev.dzt	1933 (NA)	-	512/16	60	5/30/50/56/56	1800	225	5	N

## 5. Results—Maps of All Radargrams Included in the Dataset

In this Section, we present grey-scale maps of the radargrams included in the dataset. All files generated by GPR 1 and GPR 2 were opened and displayed by using the free Matlab-based data processing software MatGPR [70]. However, this software does not open the files generated by GPR 3, which were therefore opened with commercial processing software, exported in ascii format, and then plotted with Matlab. The ascii data files are enclosed to the paper as supplementary material, so that interested researchers can easily open them without needing any commercial tool.

We have chosen to map the radargram data, directly, without applying any editing nor processing procedure. Actually, the purpose of this paper is to present the dataset and provide appropriate information about all profiles included in it, so that the scientific community can use them; our main aim is not to carry out an advanced analysis, comparison and interpretation of the data. Nonetheless, throughout this section we have accompanied the maps with several comments and considerations resulting from direct observation or from a preliminary study of the data.

Depending on the physical characteristics of the host materials, as well as on the nature, distribution and size of the buried objects, the GPR signals recorded along the eleven acquisition lines obviously vary, because they are affected by media lithology and granulometry and by the presence of scatterers. Moreover, for each acquisition line, different radargrams are of course obtained when the spectrum of the signal emitted by the radar changes. In addition, undoubtedly, different radar systems/antennas working at the same central frequency and used over the same acquisition line, provide consistent but not identical results.

Some profiles recorded with GPR 1 were pre-processed by the system before being saved, as pointed out in Section 4; by comparing pre-processed data with raw data acquired at the same frequency and over the same acquisition line, the effects of frequency-band filters application and gain recovery can be clearly appreciated. In particular, due to the geometrical spreading and attenuation of the electromagnetic waves emitted by the radar and transmitted in the subsurface, later trace arrivals in raw data show noticeably lower amplitudes than earlier arrivals; the application of a time-variant gain function allows recovering relative amplitude information (within some inevitable limits of accuracy) and allows seeing on the same grey-scale map the signatures generated by shallower and deeper objects. Moreover, the application of suitable frequency filters improves the signal-to-noise ratio.

### 5.1. Silt Region

Figures 15–20 show all radargrams gathered over the silt region, as outlined in Table 3 and in the figure captions. The frequency effect of the source is clearly notable in terms of penetration and resolution. As mentioned before, a wearing layer in limestone is present and the relevant interface is clearly visible in the maps, due to the high electromagnetic contrast, for all the central frequencies. Reflections from the lateral boundaries of the test site can be seen, too, and some diffraction signatures from the pipes and polystyrene blocks.

Regarding Figure 15, the second half of the data was collected on half line 1, over the targets, whereas the first half of the data was collected on half line 2, over the targets, too (the data of those two measurements were stored in the same file). By looking at the positions of the target signatures, it can be noticed that the data in Figures 16–20 were collected on a direction opposite to that indicated by the arrows in Figure 2 (as pointed out in Table 3). In Figure 16, the effects of the pipes buried beyond line 2 are visible in the second half of the maps, although the spatial extension of the targets does not reach line 1; such effect is obviously less notable at higher frequencies—a similar phenomenon can be noticed in several figures presented in the following Sections.

In Figure 20, the initial traces of the radargram shown in (a) have to be neglected when analyzing the data. The same is true for various radargrams of the dataset—in general, a proper number of initial traces need (almost) always to be neglected, as they correspond to data recorded above the lateral embankments. Nevertheless, such initial traces are useful for accurately locating the beginning of the



test region of interest. Similar comments apply to the final traces of the radargrams, recorded after the end of the test region of interest.

The radargram in Figure 15, recorded with GPR 1, can be compared with the radargrams in Figures 18a and 20a, recorded with GPR 3 at the same central frequency (200 MHz). The data shown in Figure 15 were pre-processed (see Table 3), whereas the data presented in Figures 18 and 20 are raw; for this reason, the signatures generated by targets and interfaces are much more visible in Figure 15. The application of suitable processing steps to the data of Figures 18 and 20 would reveal hidden information and, e.g., enable a comparison between the performances of the two radar systems and antennas. However, this would go beyond our scope and open the perspective of this paper on a number of topics that are not covered here. Analogously, the radargram in Figure 16c can be compared with the radargram in Figure 18c (and similar comments apply): they are recorded over acquisition line 1 by using GPR 1 and GPR 3, respectively, with antennas having a central frequency of 900-MHz. And, the radargram in Figure 19b can be compared with the radargram in Figure 20c: they are recorded over acquisition line 2 by using GPR 1 and GPR 3, respectively, with 900-MHz antennas.

After appropriately processing the available data, it is possible to verify that the silt region appears to be penetrated for no more than a half of its depth; the different responses of the various targets can be examined and geometrical or physical parameters of interest can be extracted (but this is not the objective of the present paper). Moreover, we implemented preliminary FDTD models of this region and by matching synthetic results with the measurements (which allows taking fully into account the wave propagation and scattering phenomena), we found that the relative permittivity of the silt is around  $\epsilon_{r,silt} = 13$ , the attenuation of the electromagnetic signal in this region of the test site is between 15 and 45 dB/m, and the penetration is about 1.5 m at the lowest frequency and 1 m at the highest. Such estimations must be taken with care, as the surface limestone layer presents some slight thickness variations, and also because of the compaction performed on the silt above the polystyrene blocks during the test site implementation (which might have compressed the blocks a little). More advanced investigations will be carried out in the future, to obtain more accurate estimations of the various values.

Still concerning the penetration depth, this parameter does not depend only on the material properties and frequency, but also on several other factors (therefore, it is not possible to calculate the conductivity of silt from the attenuation values given above). In particular, the maximum depth that a GPR can reach depends on the radar system dynamics (i.e., the minimum detectable signal-to-noise ratio), the environmental noise, the matching of the antenna to the material (i.e., the ability of the antenna to transmit electromagnetic energy in the material), the shape of the antenna radiation pattern (an antenna may focus more or less than another the electromagnetic energy in the vertical direction), the radar cross section of the targets, their spatial distribution, and the electromagnetic contrast between targets and host material (due to the scattering by the targets, the penetration depth in the test site is smaller than it would be in a target-free scenario).

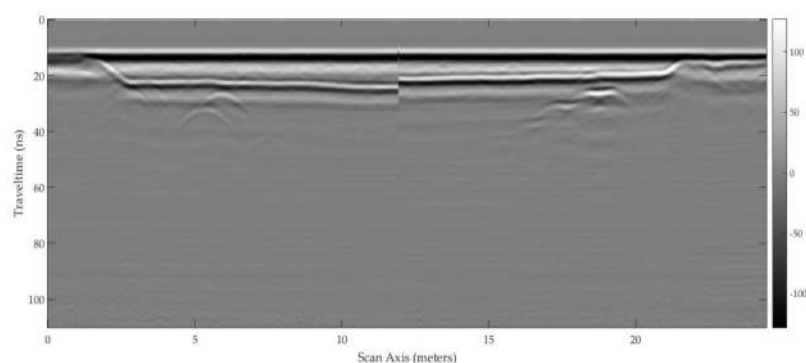


**Figure 15.** Profile recorded in the silt region by using GPR 1, on acquisition lines 1 and 2, with an antenna operating at the central frequency of 200 MHz.

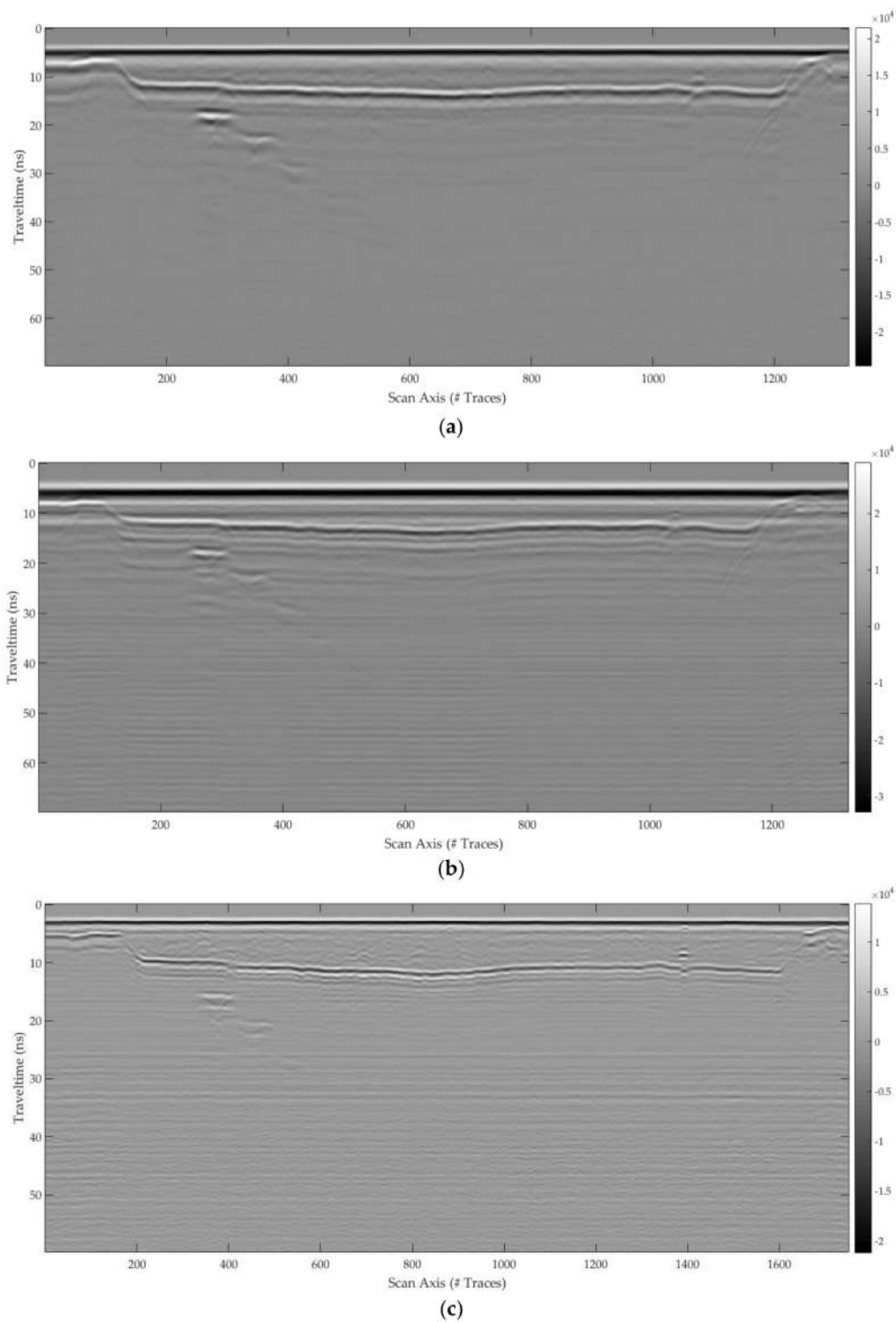


**Figure 16.** Profiles recorded in the silt region by using GPR 1, on acquisition line 1, with antennas operating at the following central frequencies: (a) 400 MHz; (b) 500 MHz; (c) 900 MHz. Data recorded at 200 MHz are shown in Figure 15.

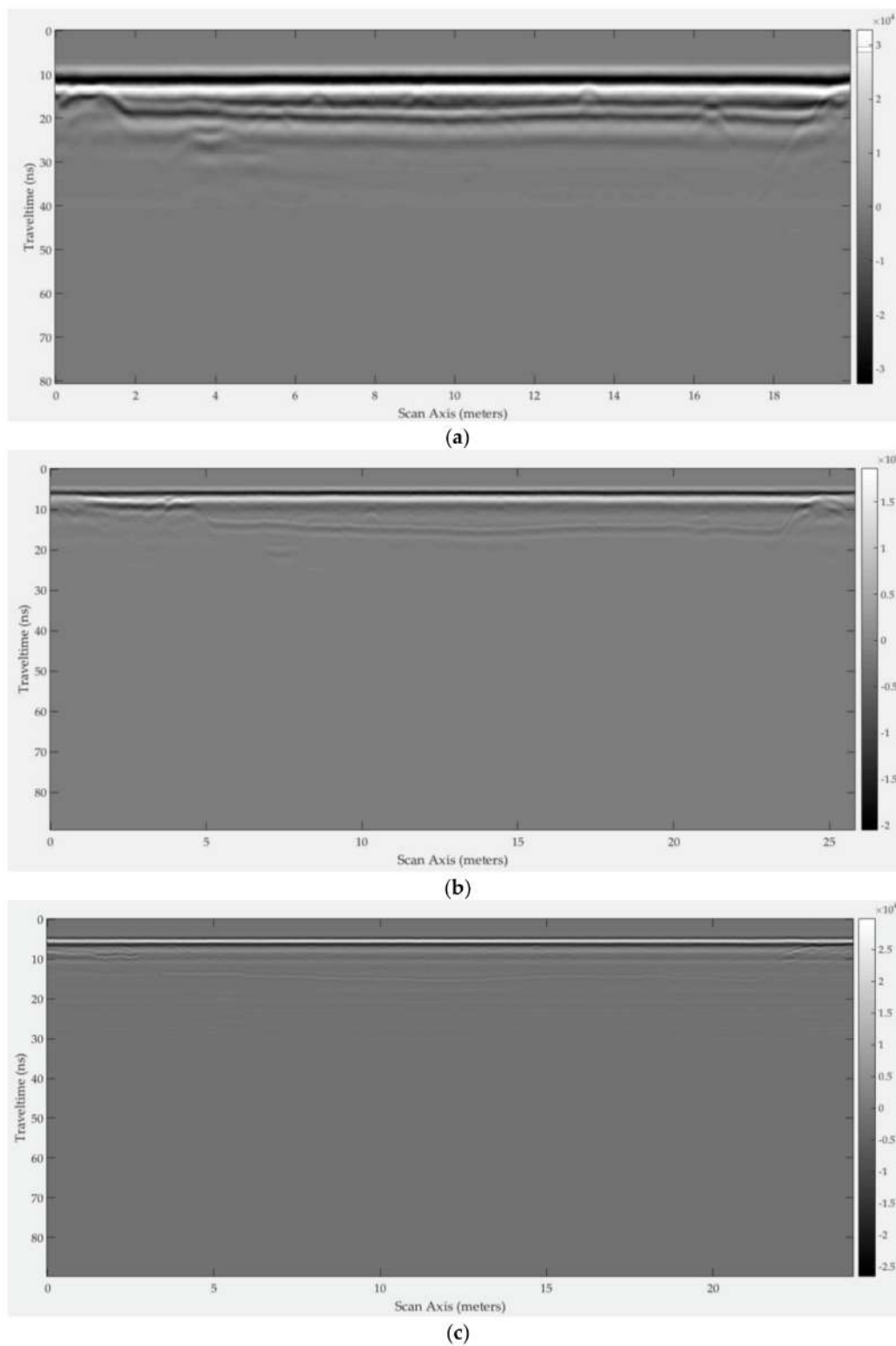


**Figure 17.** Profiles recorded in the silt region by using GPR 2, on acquisition line 1, with antennas operating at: (a) 250 MHz; (b) 500 MHz; (c) 800 MHz.

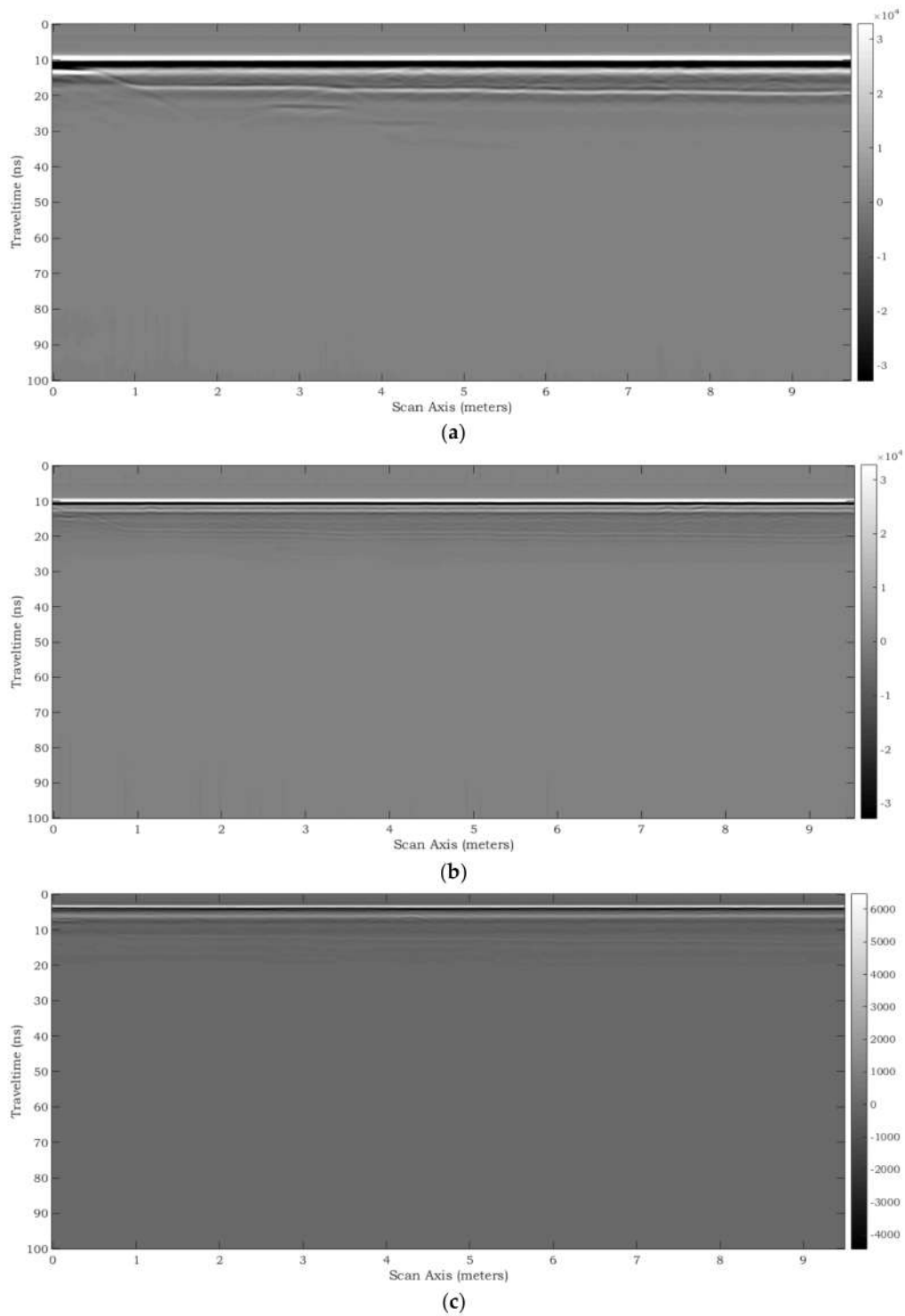
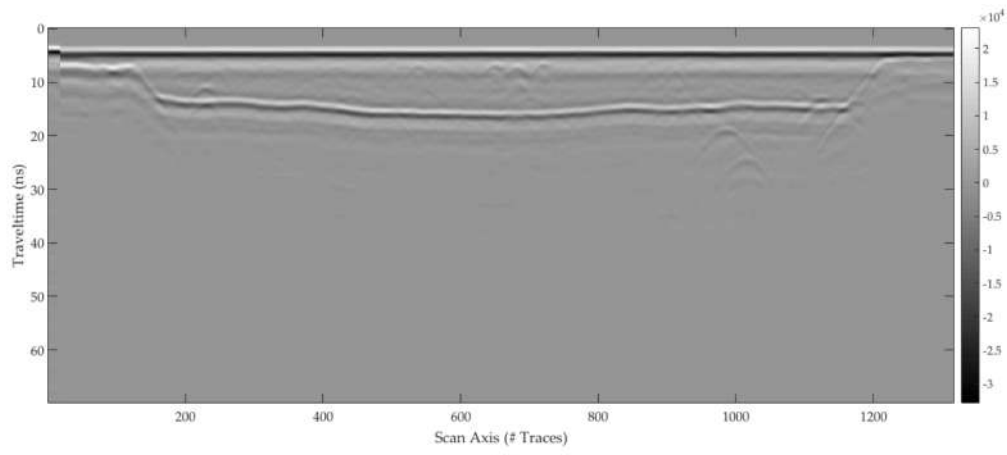
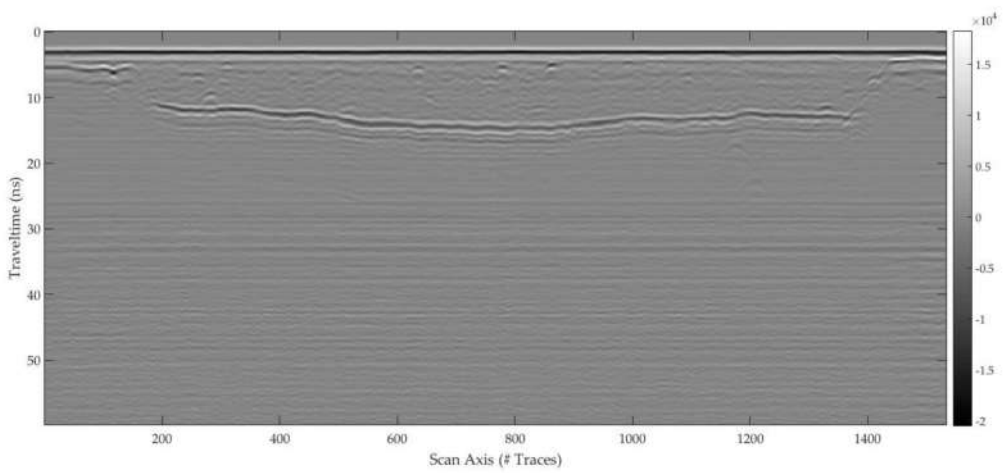


**Figure 18.** Profiles recorded in the silt region by using GPR 3, on acquisition line 1, with antennas operating at: (a) 200 MHz (data collected over a 9.7 m long portion of the acquisition line); (b) 600 MHz (9.52 m long portion of the acquisition line); (c) 900 MHz (9.48 m long portion of the acquisition line).



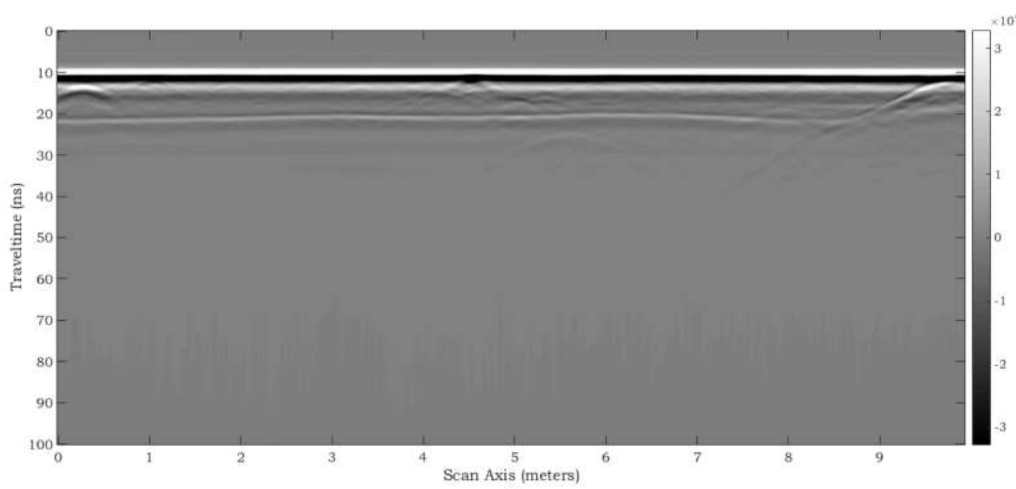


(a)



(b)

**Figure 19.** Profiles recorded in the silt region by using GPR 1, on acquisition line 2, with antennas operating at: (a) 400 MHz; (b) 900 MHz. Data recorded at 200 MHz are in Figure 15.



(a)

**Figure 20.** Cont.

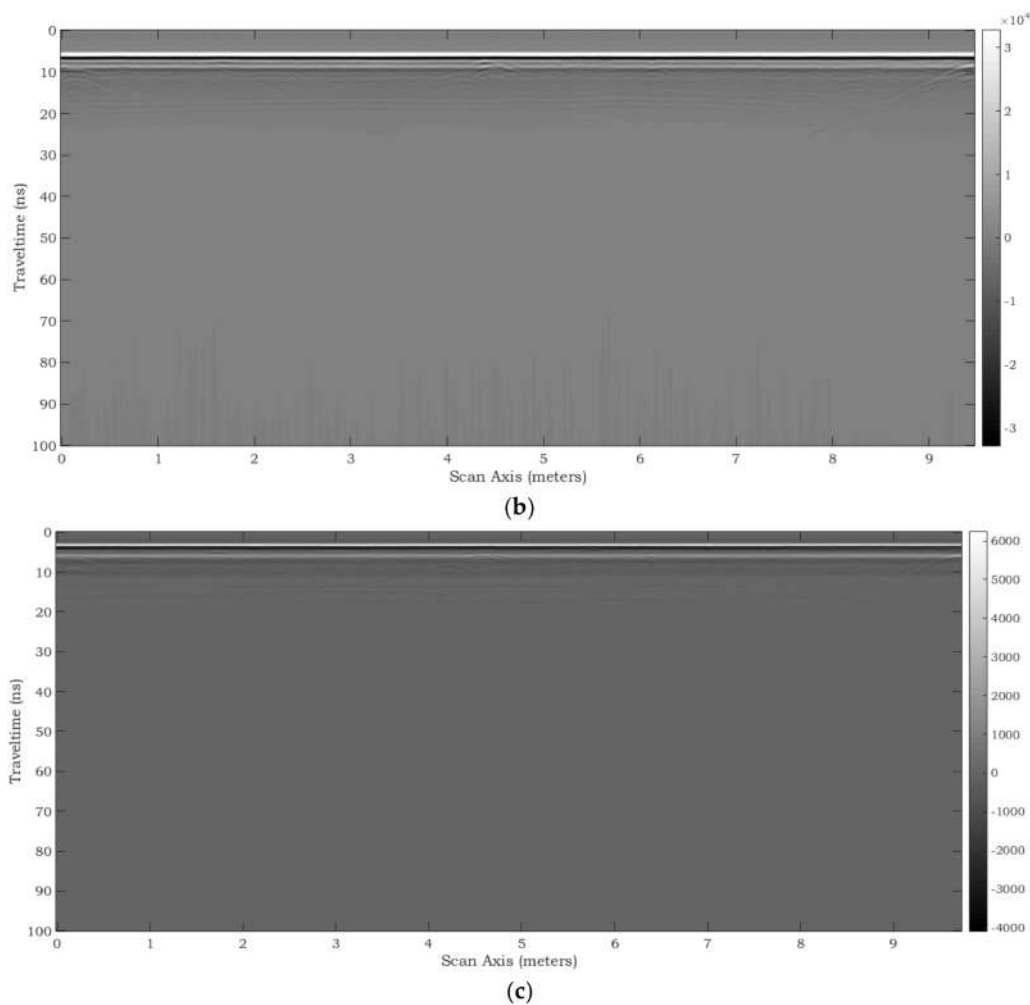


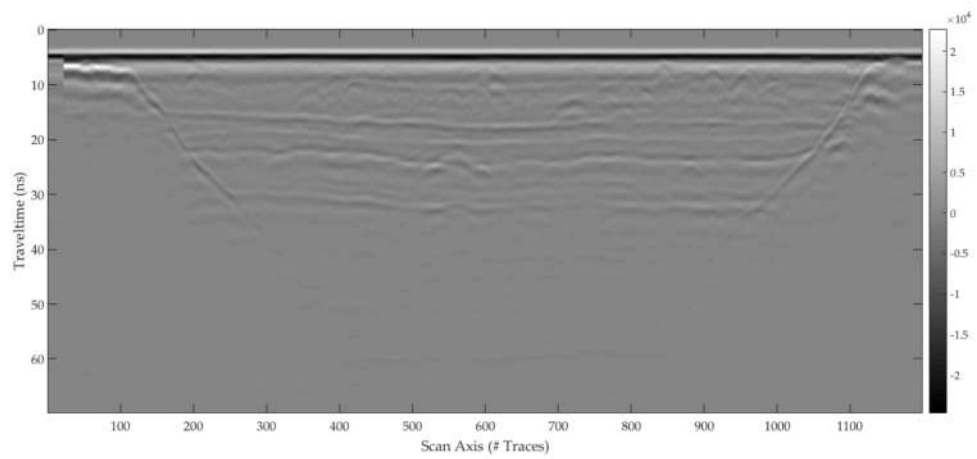
**Figure 20.** Profiles recorded in the silt region by using GPR 3, on a portion of acquisition line 2, with antennas operating at: (a) 200 MHz (9.92 m long); (b) 600 MHz (9.48 m long); (c) 900 MHz (9.72 m long).

## 5.2. Multilayer

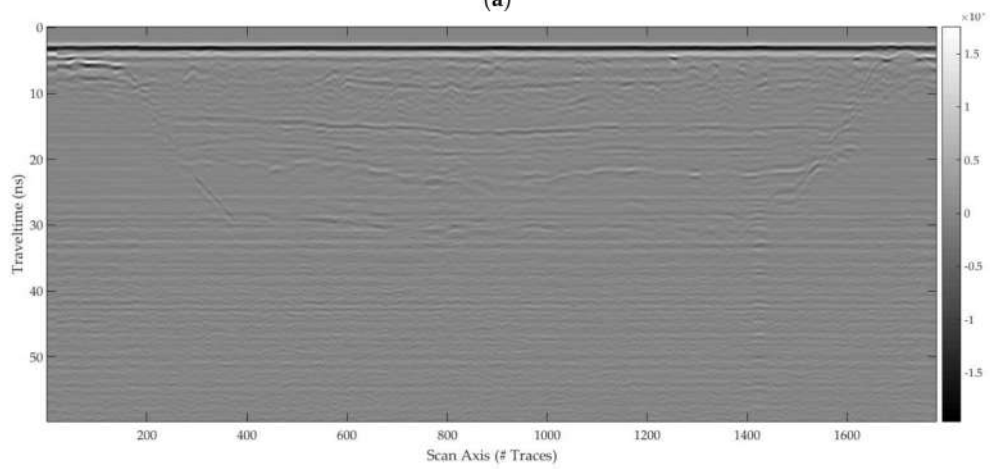
Figures 21 and 22 show the radargrams collected over the multilayer, as outlined in Table 4 and in the figure captions. The multi-layer section is the only one that was not geo-localized during the implementation of the test site. Then, the thicknesses of every layer remain theoretical.

While studying the GPR profiles (e.g., Figure 21a), several findings can be made. For example, concerning the practical implementation of the layers, despite great precautions to realize homogeneous layers were taken, an elementary ~25-cm implementation of soil sub-layers followed by compaction remains visible due to slight electromagnetic contrasts. A further comment is related to the double travel times in the two layers of gneiss: as the Gneiss 14/20 material presents a high level of porosity (due to the lack of fine and small elements), the corresponding GPR velocity is faster than for Gneiss 0/20 and this should induce different thicknesses for these two Gneiss layers, which are declared similar (60 cm). One possible explanation could be from an unwanted filling of Gneiss 14/20 by fine and small elements of Gneiss 0/20, due to gravity and opened voids in the Gneiss 14/20 skeleton; but this explanation remains only partial. Another observation is associated with GPR scattering phenomena occurring in the upper limestone layer, due to the presence of big coarse aggregates that remained there, although they should have been removed.

The multilayer section remains a challenge for GPR specialists, to estimate the real thicknesses and permittivity values of the various layers.

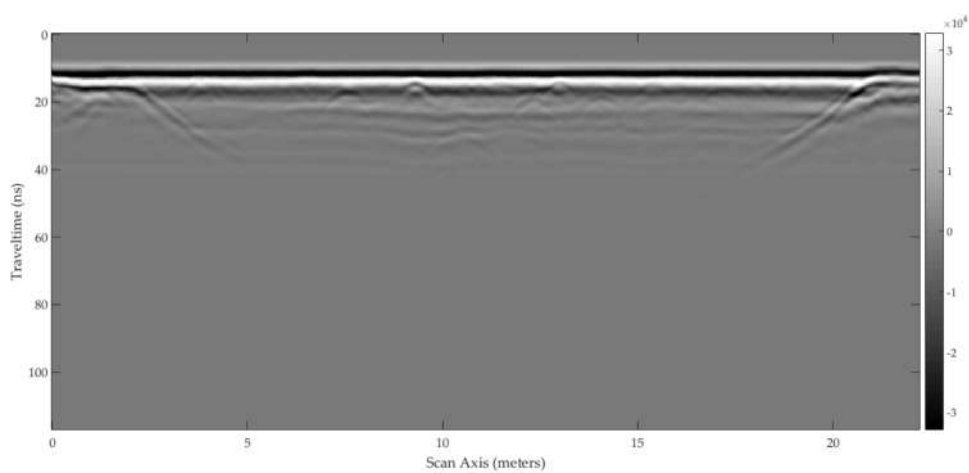


(a)



(b)

**Figure 21.** Profiles recorded in the multilayer by using GPR 1, with antennas operating at: (a) 400 MHz; (b) 900 MHz.



(a)

**Figure 22.** Cont.

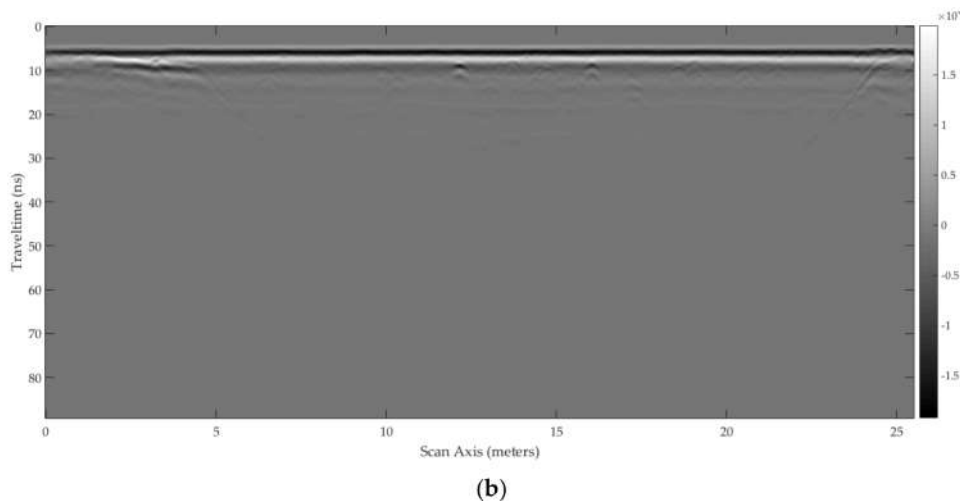


**Figure 22.** Profiles recorded in the multilayer by using GPR 2, with antennas operating at: (a) 250 MHz; (b) 500 MHz.

### 5.3. Limestone Region

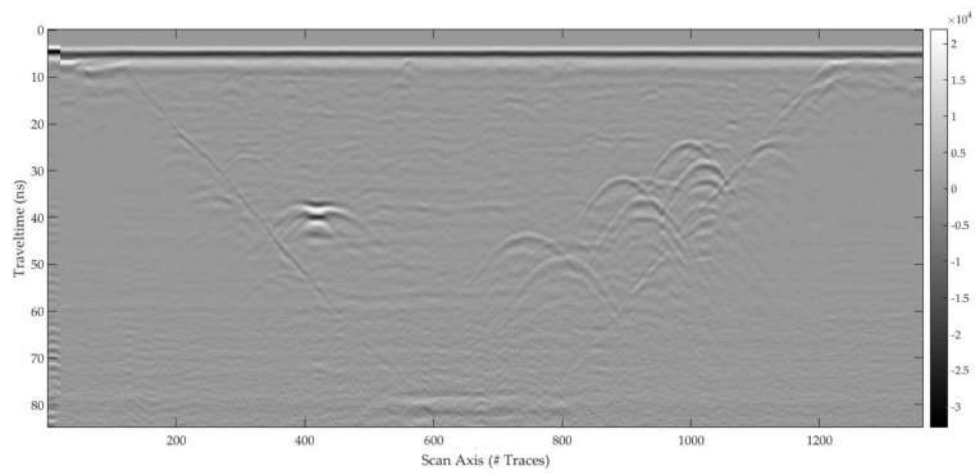
Figures 23–28 show the radargrams gathered over the limestone region, as outlined in Table 5 and in the figure captions. Some radargrams were collected on a direction opposite to that indicated by the arrows in Figure 2, as pointed out in Table 5.

For GPR 1 and acquisition line 2, two different radargrams are available for the central frequency of 400 MHz, collected with an older and a newer antenna (they are shown in Figures 24b and 26a, respectively); the same is true for the central frequency of 900 MHz (Figures 24c and 26b). The radargram in Figure 24a, recorded with GPR 1 over acquisition line 2 at 200 MHz, can be compared with the radargram in Figure 28a, recorded with GPR 3 over the same acquisition line and at the same frequency. Analogously, Figures 24c and 26b can be compared with Figure 28c.

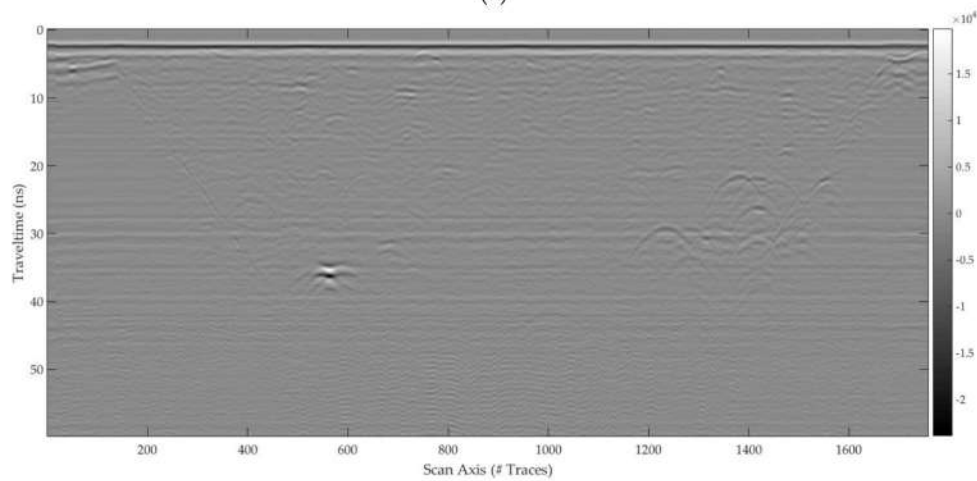
Several observations can be done by studying these maps. This region is particularly interesting for GPR surveys, as the medium is realistic, homogeneous and electromagnetically resistive. As a consequence, one can detect the sides of the test site and its bottom, constituted by a drainage layer and two lateral drainage pipes. The response to the heterogeneities also merits some comments. Every target is clearly detected, such as the polystyrene block (well visible, in Figure 23a–b), which borders generate hyperbolas, or the polystyrene cavity (see Figure 24a–b), and most of the nine pipes. As is well known, the interaction of electromagnetic fields with scatterers strongly depends on their size compared to wavelength. When objects are sufficiently large, such as the polystyrene block and cavity, the interpretation of their signatures in the radargrams is easier and the reflected signal contains complete information about their shape. On the contrary, when objects are small compared to wavelength, they are still detectable but more difficult to characterize, for example it is not trivial to estimate the size of the pipes—especially at lower frequencies. However, it is interesting to observe how pipes of different nature can be distinguished thanks to the differences between their signatures: a steel pipe generates a single hyperbola; a PVC pipe filled with water generates a first hyperbola coming from the upper side of the pipe and successive hyperbolas due to the reflections coming from its bottom (echoes which amplitude is stronger than for the first one); an empty PVC pipe also generates reflections from both its upper side and bottom, but the pattern is different, because the velocity of electromagnetic fields in air is higher than in water, and so the successive echoes are more discernible for the PVC pipe filled with water than for the empty one.

By analyzing the data and implementing preliminary FDTD models of this region, it is reasonable to assume that the relative permittivity of limestone is around  $\epsilon_{r,sand} = 6$ , the attenuation of the electromagnetic signal is between 6 and 20 dB/m, the penetration is at least 4.5 m at the lowest

frequency (the bottom of the pit is visible) and 2 m at the highest. Further studies are necessary for a more accurate estimation of these values.

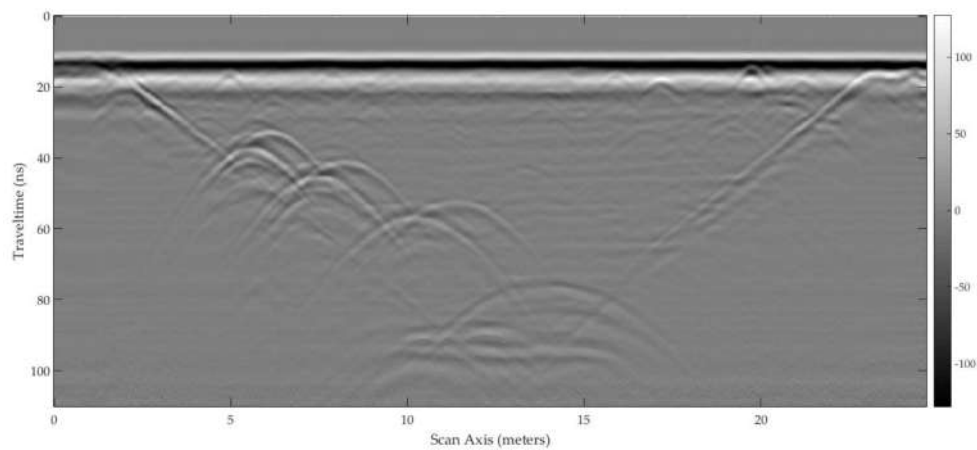


(a)



(b)

**Figure 23.** Profiles recorded in the limestone region by using GPR 1, on acquisition line 1, with antennas operating at: (a) 400 MHz; (b) 900 MHz.



(a)

**Figure 24.** Cont.

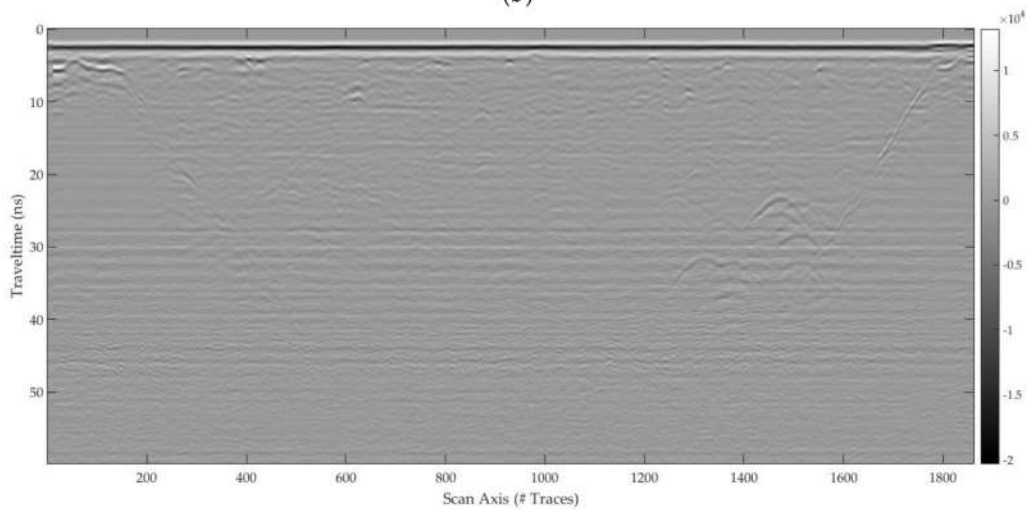
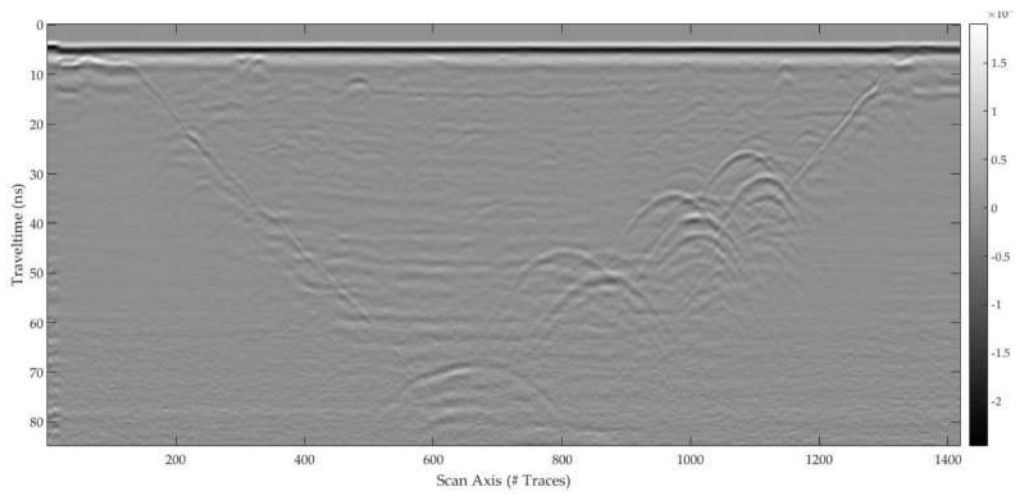


**Figure 24.** Profiles recorded in the limestone region by using GPR 1, on acquisition line 2, with antennas operating at: (a) 200 MHz; (b) 400 MHz; (c) 900 MHz.

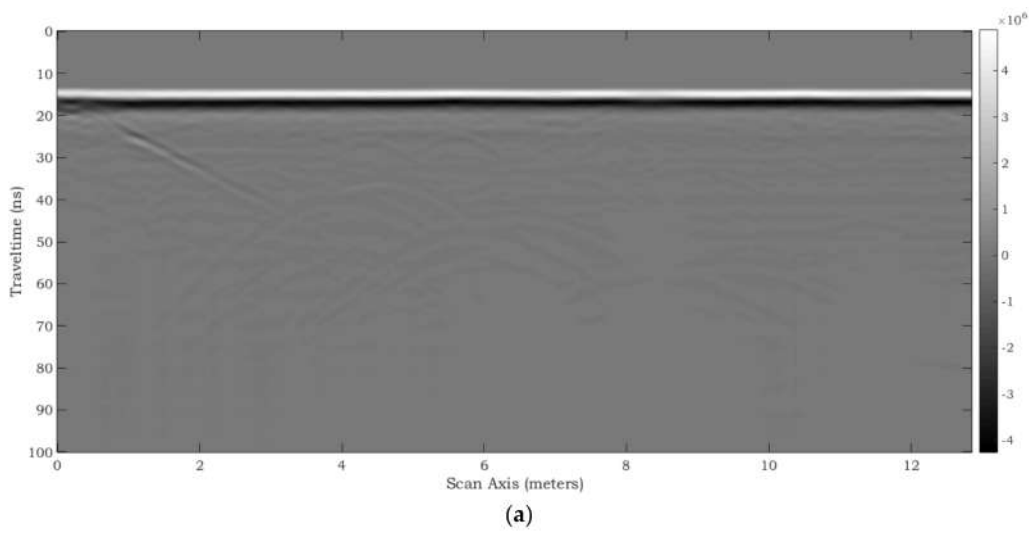


**Figure 25.** Cont.



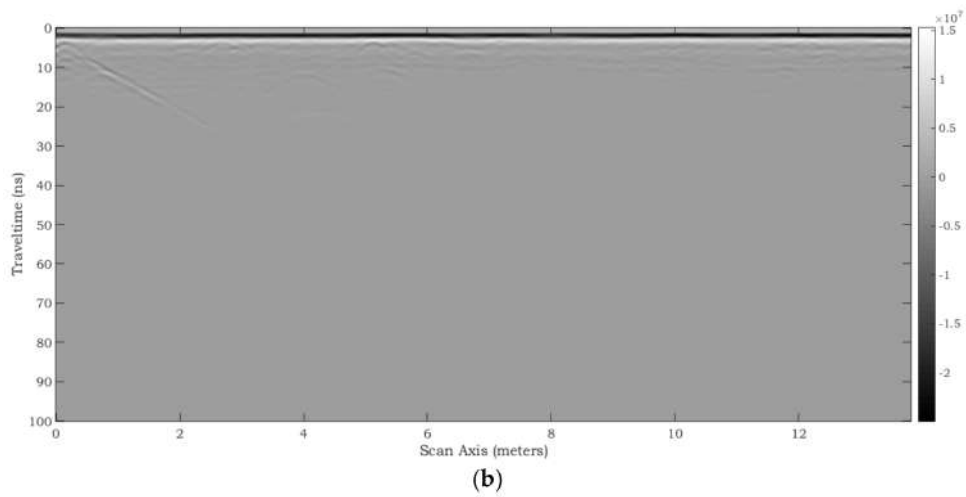


**Figure 25.** Profiles recorded in the limestone region by using GPR 1, on acquisition line 2, with antennas operating at: **(a)** 270 MHz; **(b)** 350 MHz.

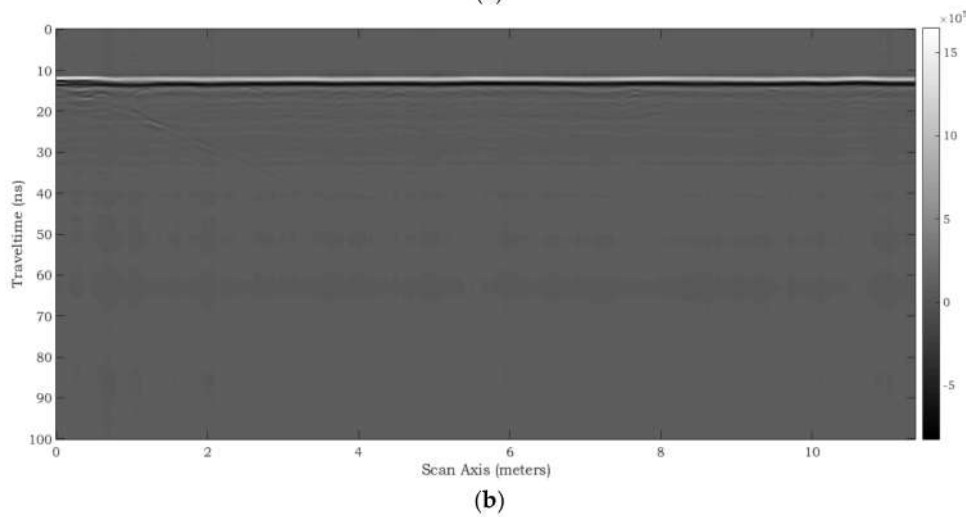
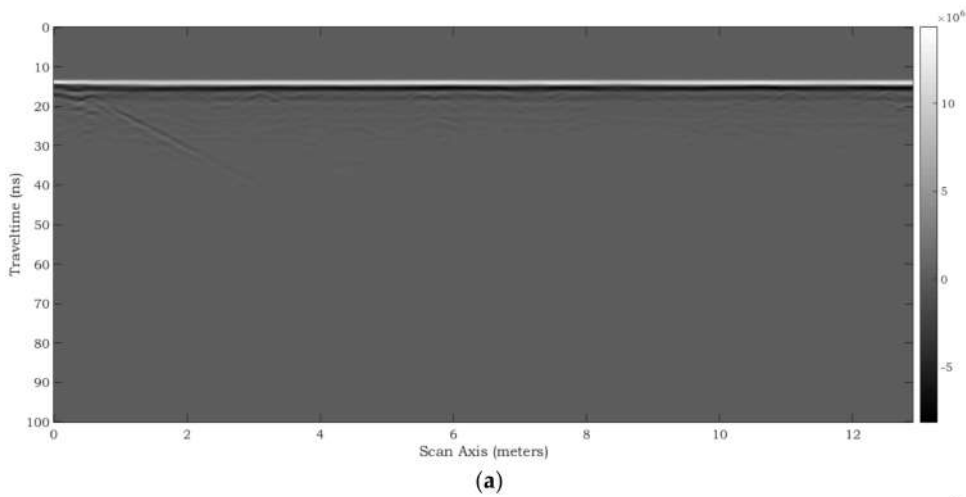
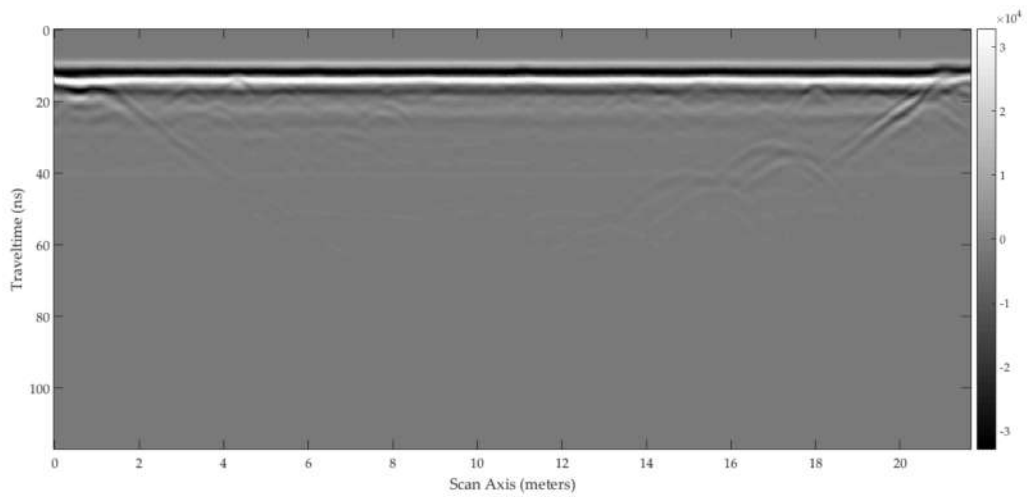
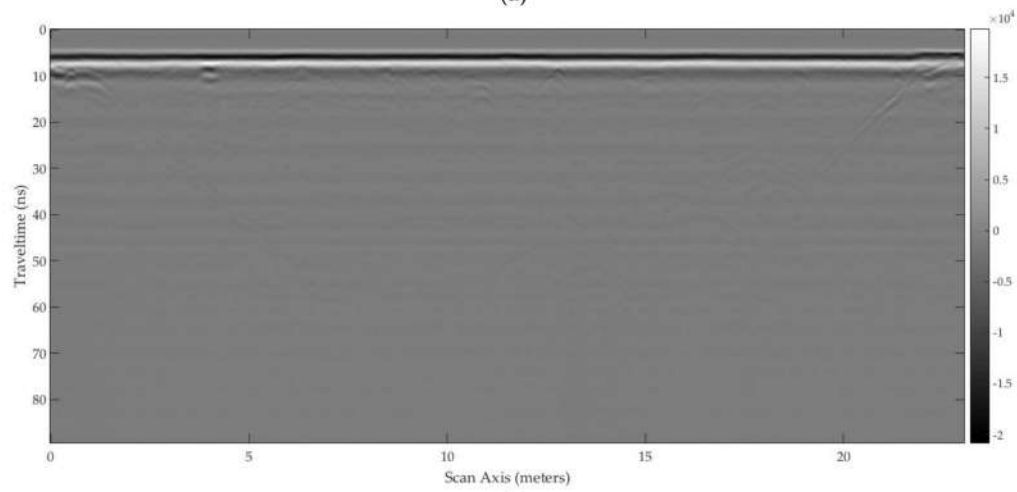


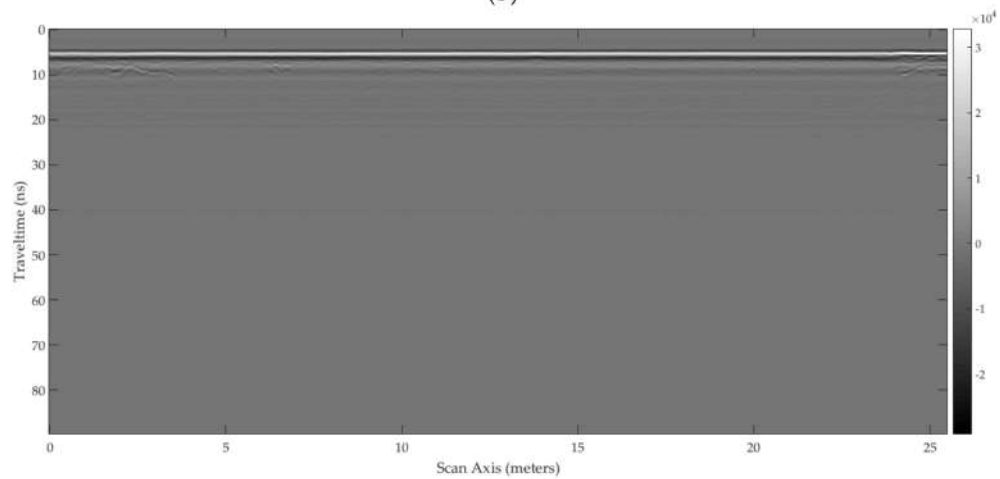
**Figure 26.** Profiles recorded in the limestone region by using GPR 1, on acquisition line 2, with ‘new’ antennas operating at: **(a)** 400 MHz; **(b)** 900 MHz.



(a)



(b)



(c)

**Figure 27.** Profiles recorded in the limestone region by using GPR 2, on acquisition line 2, with antennas operating at: (a) 250 MHz; (b) 500 MHz; (c) 800 MHz.

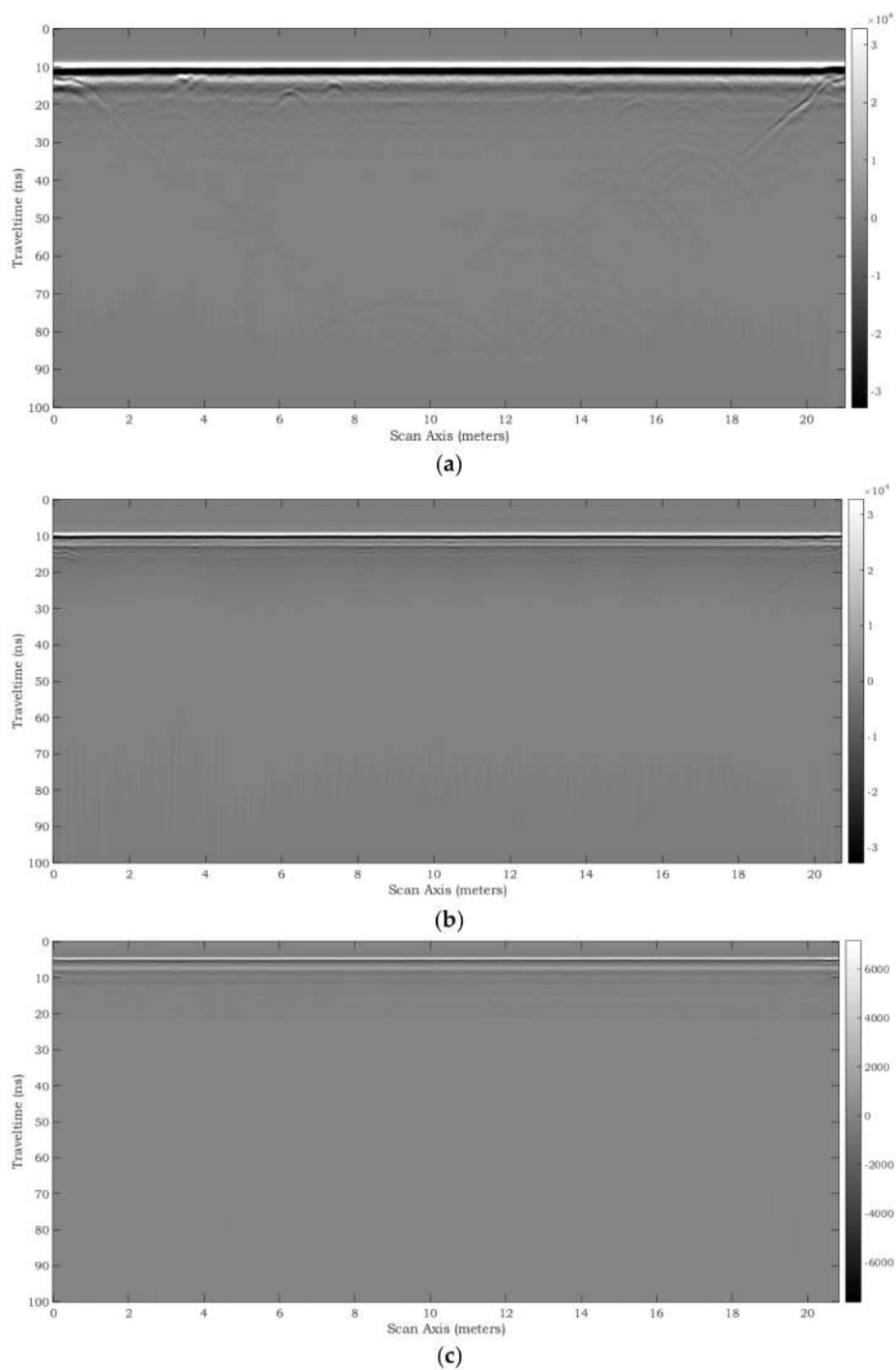


**Figure 28.** Profiles recorded in the limestone region by using GPR 3, on acquisition line 2, with antennas operating at: (a) 200 MHz; (b) 600 MHz; (c) 900 MHz.

#### 5.4. Gneiss 14/20 Region

Figures 29–34 show the radargrams gathered over the Gneiss 14/20 gravel region, as outlined in Table 6 and in the figure captions. Some radargrams were collected on a direction opposite to that indicated by the arrows in Figure 2, as pointed out in Table 6.

For this section of the test site, the richness of the dataset allows performing various comparisons between radargrams recorded with different equipment working at the same central frequency.

This region was especially designed to propose an artificial lossless medium for GPR-operator beginners in training. Figure 31a is probably the radargram of the dataset that is easiest to read, as it is almost noiseless; this case, along with the results obtained by using the same system at higher frequencies, can be an excellent starting point for testing modeling, imaging, inversion and processing algorithms and it is also particularly good for teaching purposes. The bottom of the pit and all the buried objects are well visible in Figure 31a. The big concrete pipe generates two hyperbolas, which indicate its top and base and allow estimating its size. In the center of the radargram, it is possible to notice several reflections, which are due to the almost-parallel and almost-horizontal interfaces between compaction sub-layers. It is also interesting to observe the two hyperbolas generated by the wedges at the bottom of the site (i.e., where the sloping sides of the pit reach its base and two drains are present). For the signatures generated by the three layers of steel and PVC pipes, comments similar to those written in Section 5.3 apply.

By analysing the data and implementing preliminary FDTD models of this region, it is reasonable to assume that the relative permittivity is around  $\epsilon_{r,g1420} = 3$ , the attenuation of the electromagnetic signal is between 1.5 and 4.5 dB/m (this is the region with lowest attenuation), and the penetration is at least 4.5 m at all considered frequencies (meaning that the bottom of the pit can always be seen). Further studies will provide a more accurate estimation of these values.

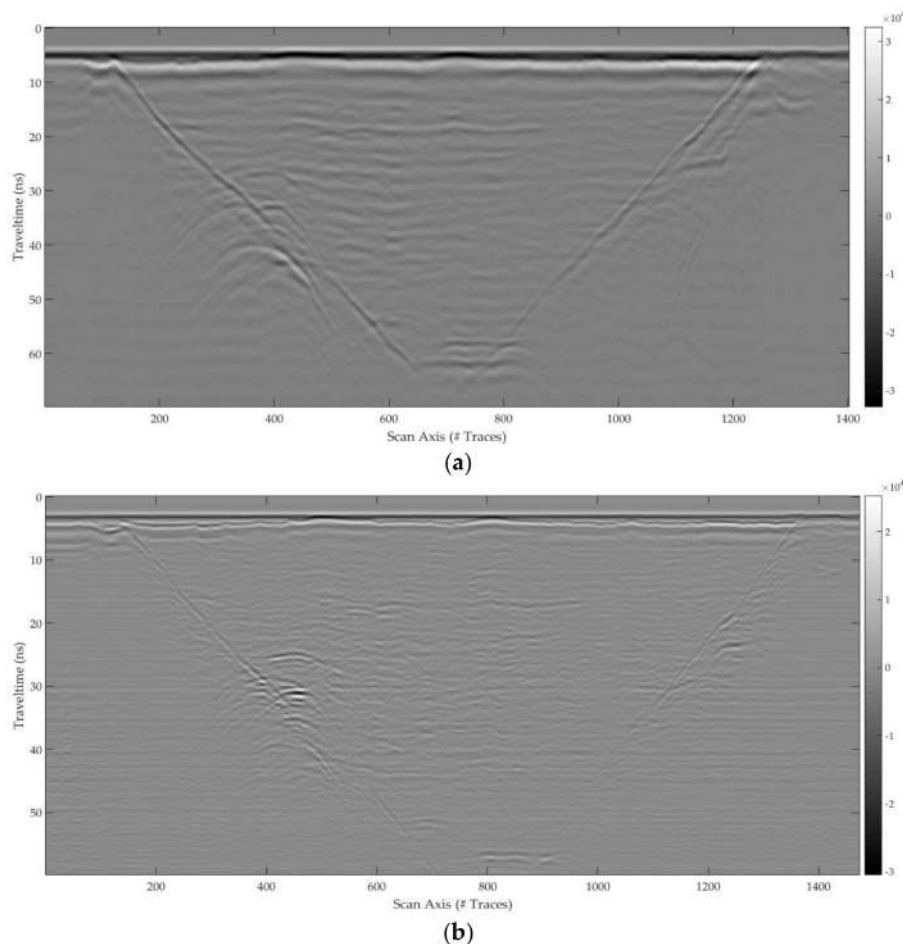


**Figure 29.** Profiles recorded on acquisition line 1 of the Gneiss 14/20 gravel region by using GPR 1 and antennas operating at: (a) 400 MHz; (b) 900 MHz.

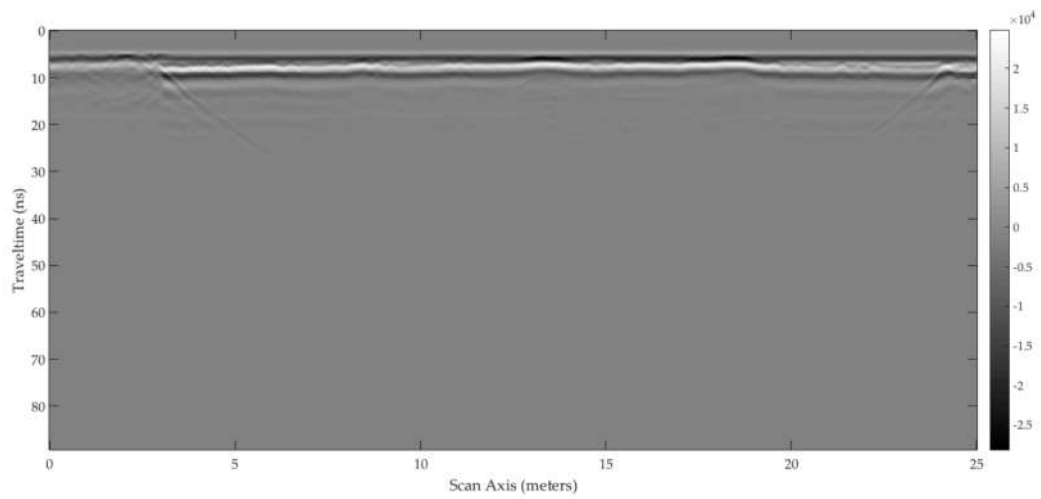
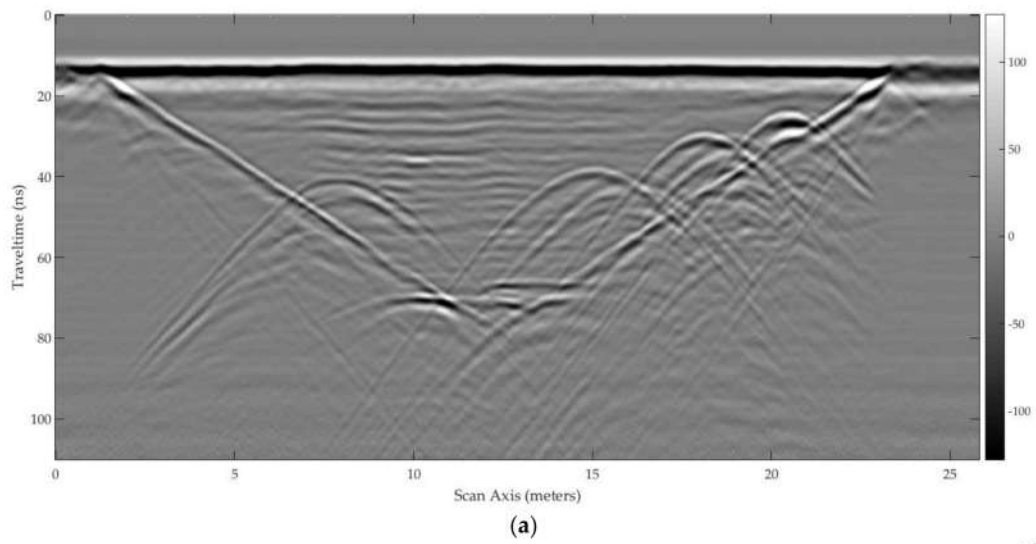
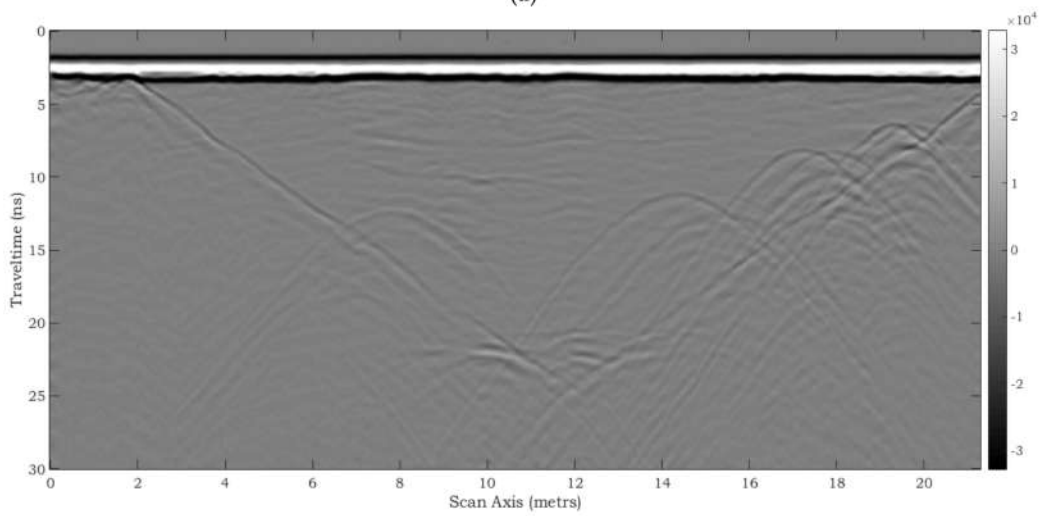


**Figure 30.** Profile recorded on acquisition line 1 of the Gneiss 14/20 gravel region by using GPR 2 and a 500-MHz antenna.



(a)



(b)

**Figure 31.** Cont.

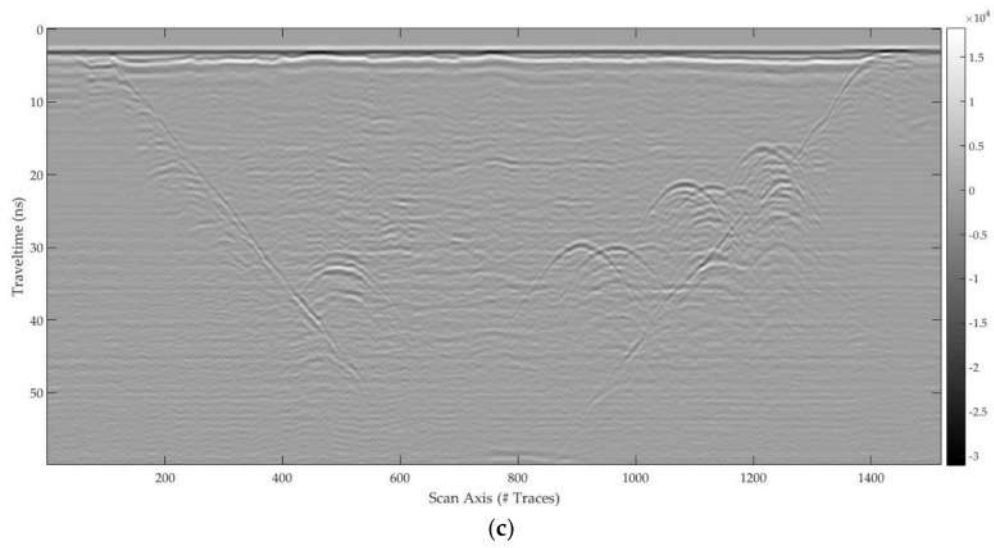


**Figure 31.** Profiles recorded in the Gneiss 14/20 gravel region by using GPR 1, on acquisition line 2, with antennas operating at: (a) 200 MHz; (b) 400 MHz; (c) 900 MHz.

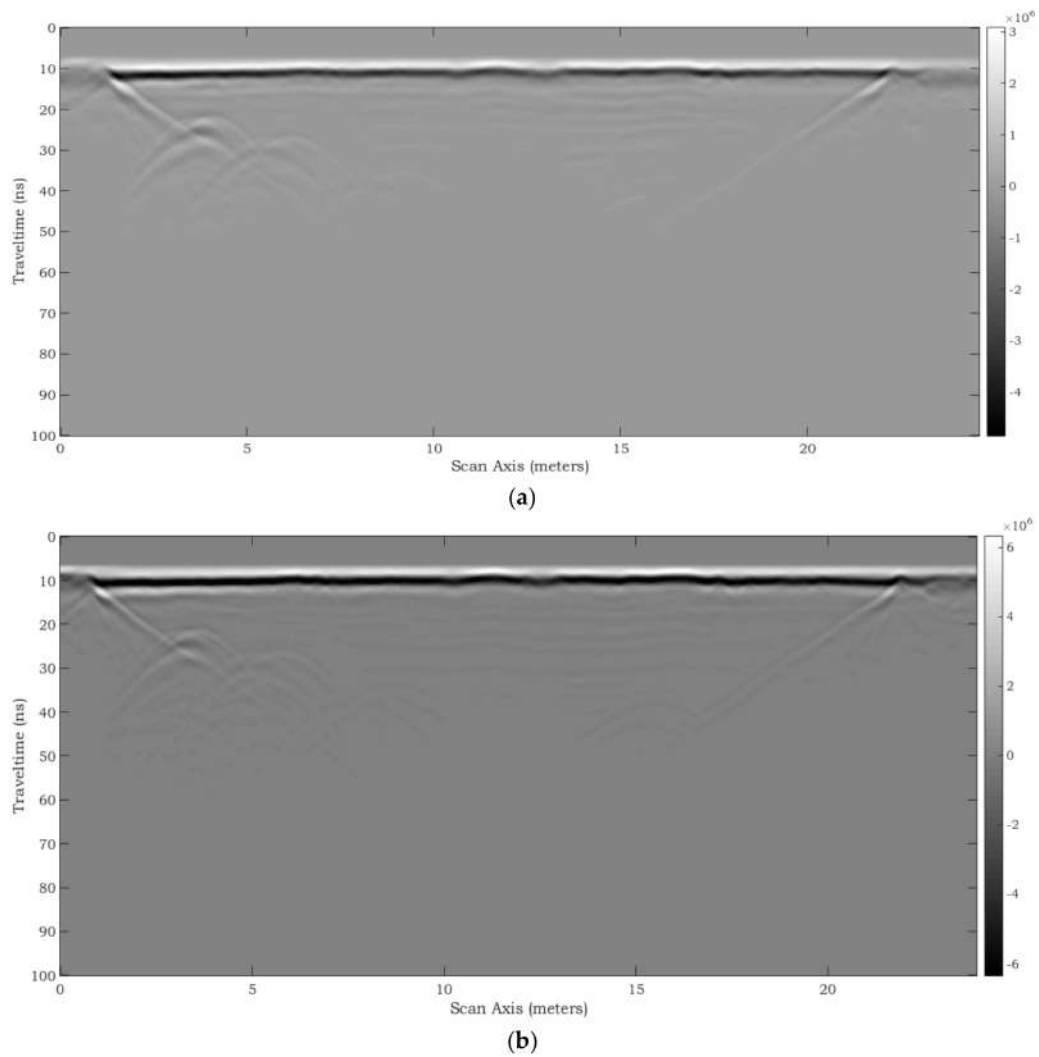


**Figure 32.** Cont.



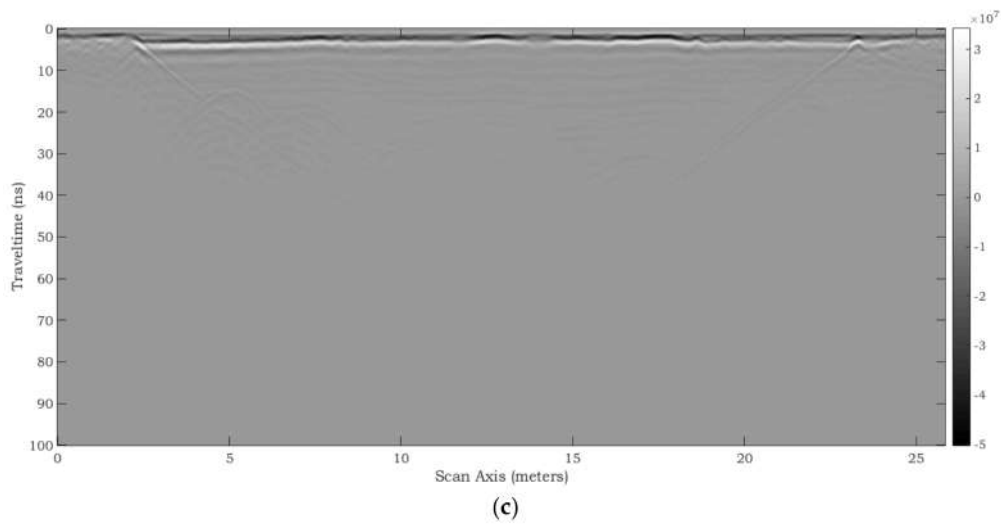


**Figure 32.** Profiles recorded in the Gneiss 14/20 gravel region by using GPR 1, on acquisition line 2, with ‘new’ antennas operating at: (a) 200 MHz; (b) 270 MHz; (c) 350 MHz.

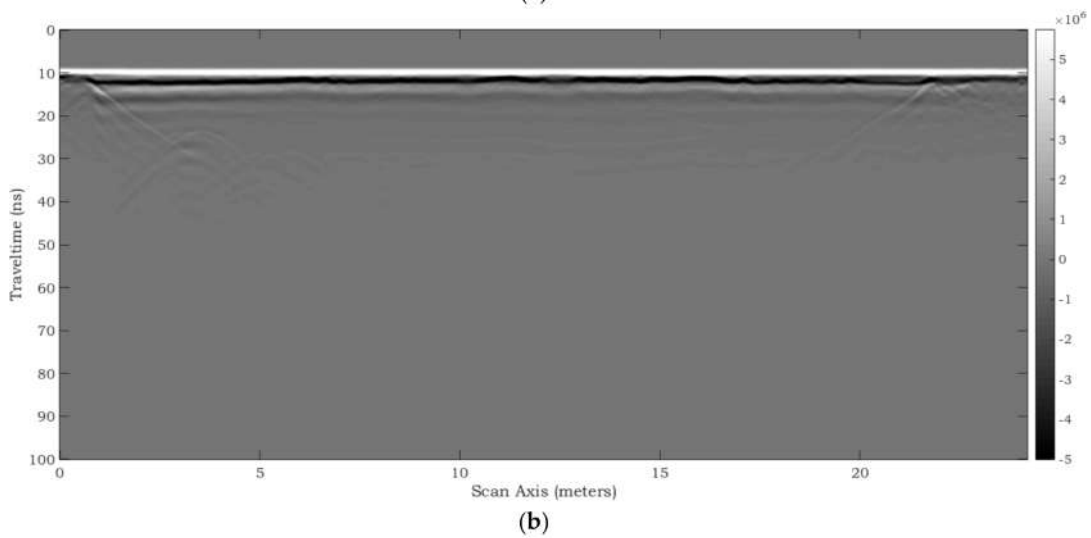
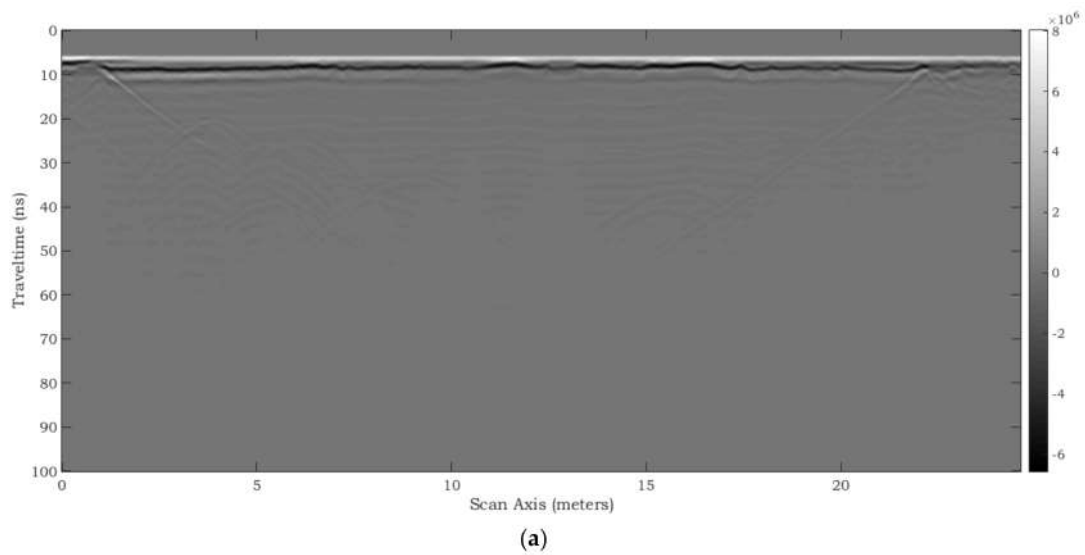


**Figure 33.** Cont.

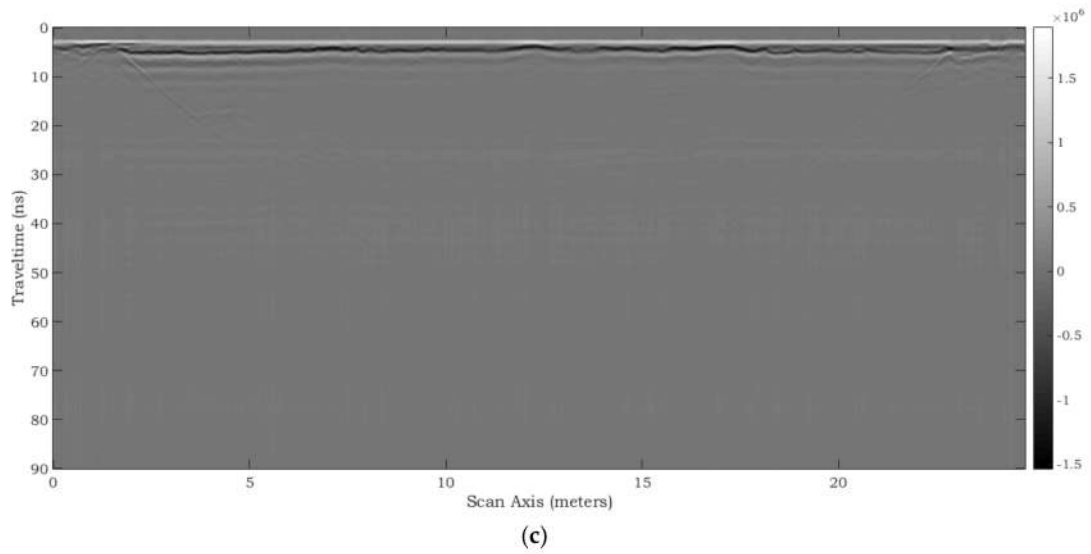


**Figure 33.** Profiles recorded in the Gneiss 14/20 gravel region by using GPR 1, on acquisition line 2, with last-generation antennas operating at: (a) 400 MHz; (b) 500 MHz; (c) 900 MHz.

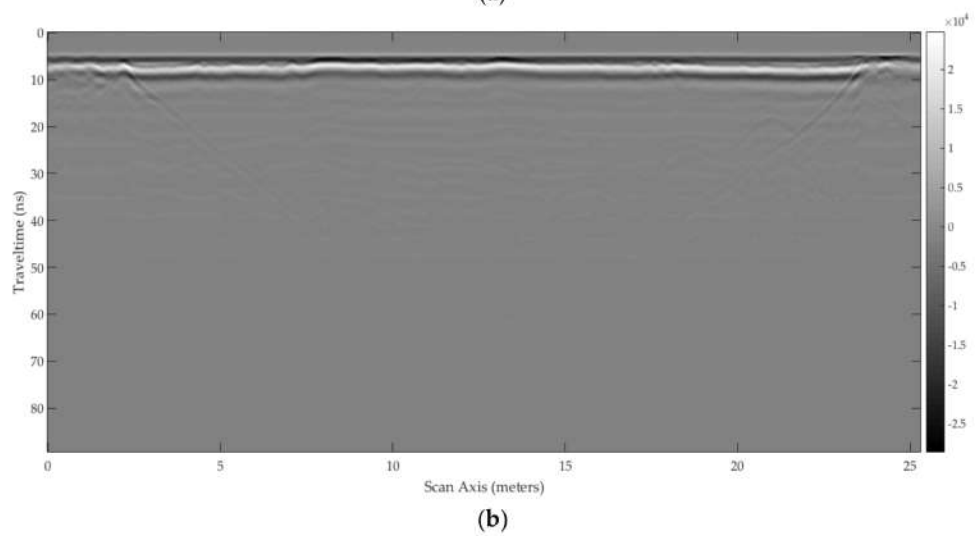
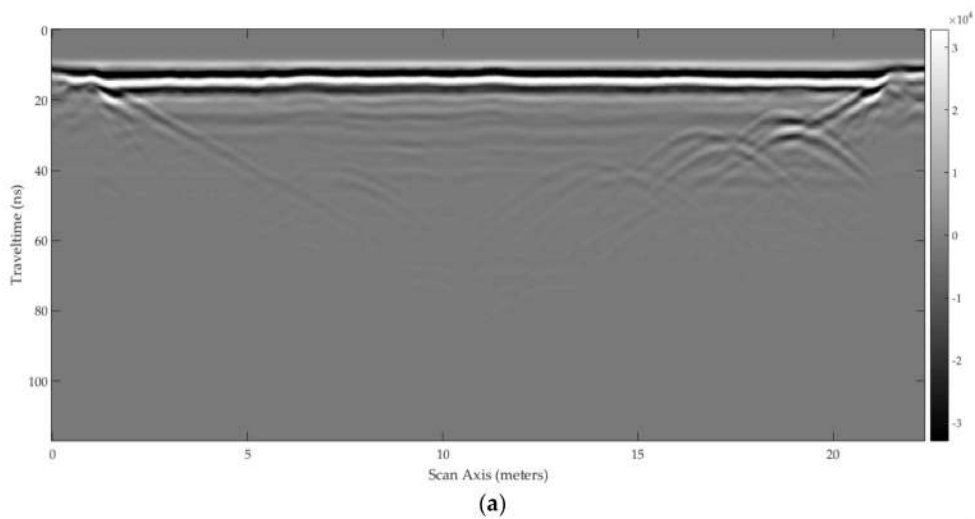


**Figure 34.** Cont.

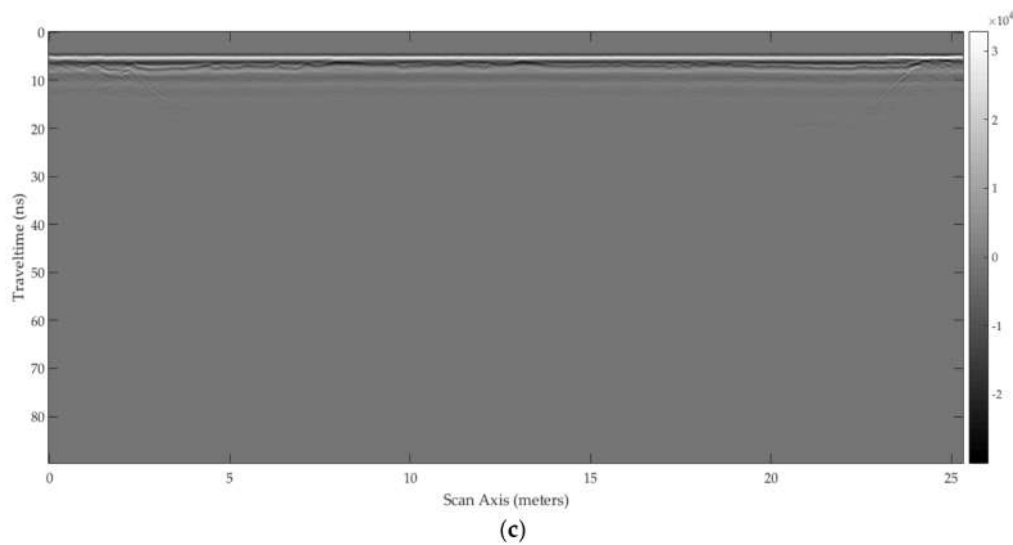


**Figure 34.** Profiles recorded in the Gneiss 14/20 gravel region by using GPR 2, on acquisition line 2, with antennas operating at: (a) 250 MHz; (b) 500 MHz; (c) 800 MHz.

### 5.5. Gneiss 0/20 Region

Finally, Figures 35–42 show the radargrams gathered over the Gneiss 0/20 gravel region, as outlined in Table 7 and in the figure captions.

For acquisition line 1, various comparisons are possible between radargrams collected by using different equipment working at the same central frequency.

The high-density gravel turned out to be so strongly absorbing that the girder is very difficult to detect. A comparison between the radargrams recorded in this region and those recorded in the gneiss 14/20 region, proves how strong is the influence of the fine fractions present on the 0/20 scale: they cause the permittivity of the medium and signal attenuation to be much higher and so prevent any deep penetration of the electromagnetic waves into the ground. Reflections generated by the almost-parallel and almost-horizontal interfaces between compaction sub-layers are visible in the radargrams, same as already commented for the radargrams presented in the previous sub-section: let us now additionally mention that, on one hand, such reflections prove the very high sensitivity of the GPR technique, which is capable to detect interfaces between regions of same material only because they were separately compacted, as well as how large is the amount of information that can be extracted from GPR data; on the other hand, those reflections suggest how difficult the interpretation of GPR data can be, especially in variegated urban scenarios where the measurements can be quite noisy due to the inhomogeneity of the subsurface and to the presence of stones or other scattering elements.

By analyzing the data and implementing preliminary FDTD models of this region, it is reasonable to assume that the relative permittivity is around  $\epsilon_{r,g0020} = 5.5$ , the attenuation of the electromagnetic signal is between 9 and 27 dB/m, the penetration is about 2.5 m at the lowest frequency and 1.5 m at the highest. Further studies are necessary for a more accurate estimation of these values.

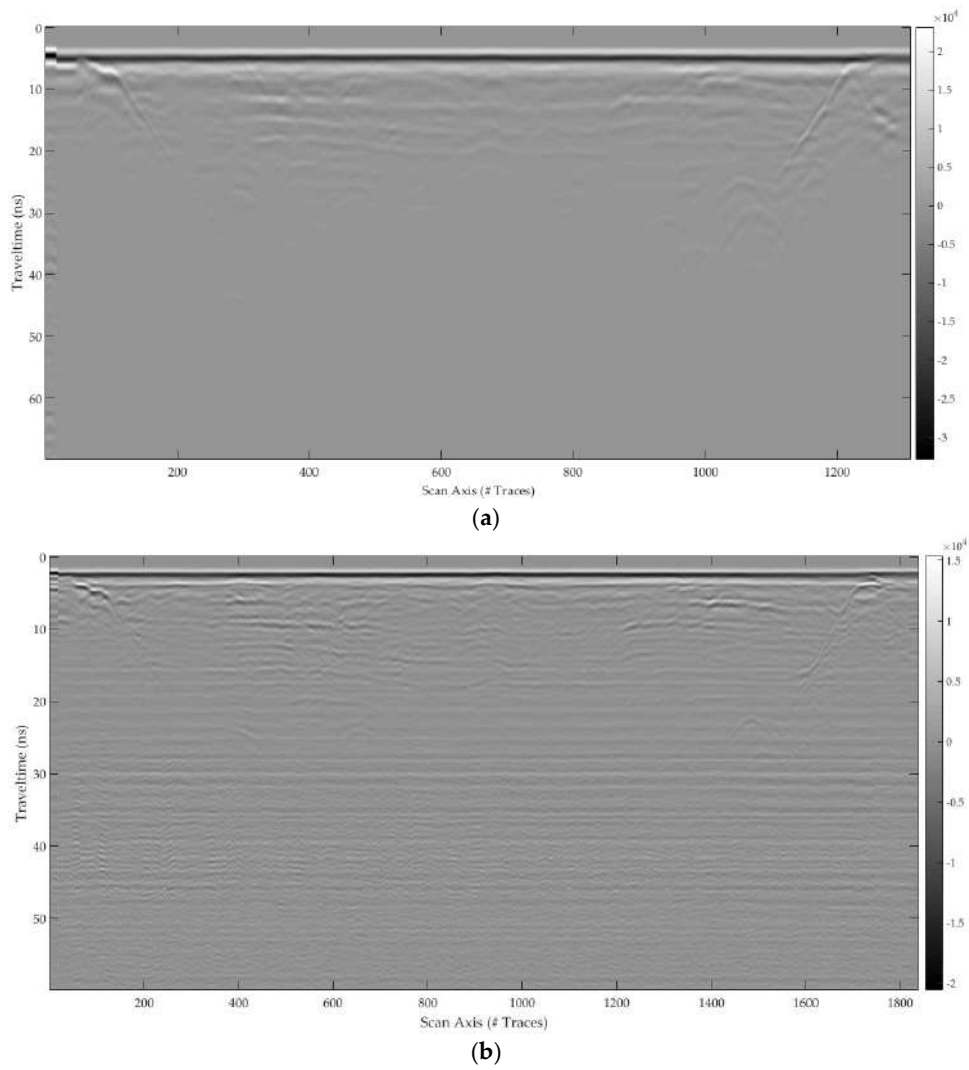


**Figure 35.** Profiles recorded in the Gneiss 0/20 gravel region by using GPR 1, on acquisition line 1, with antennas operating at: (a) 400 MHz; (b) 900 MHz.

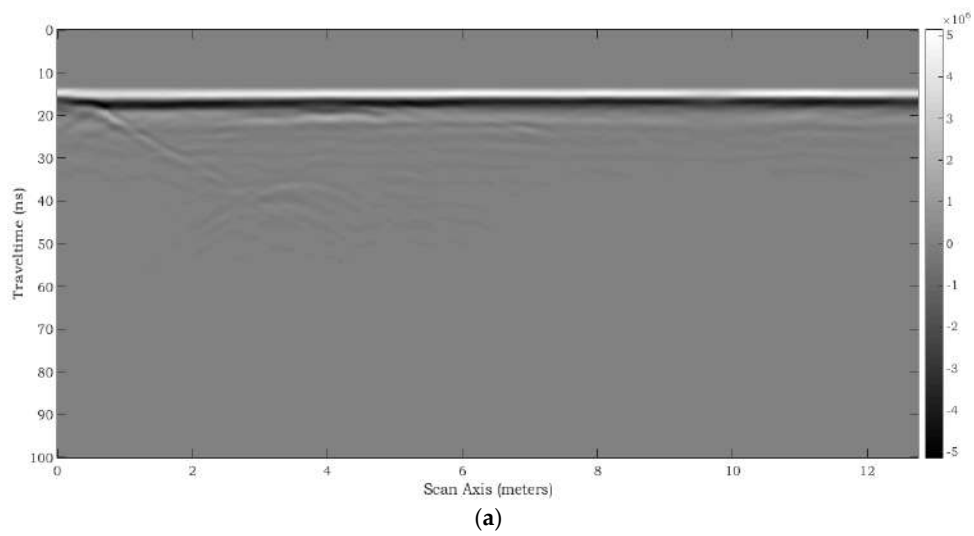


**Figure 36.** Cont.

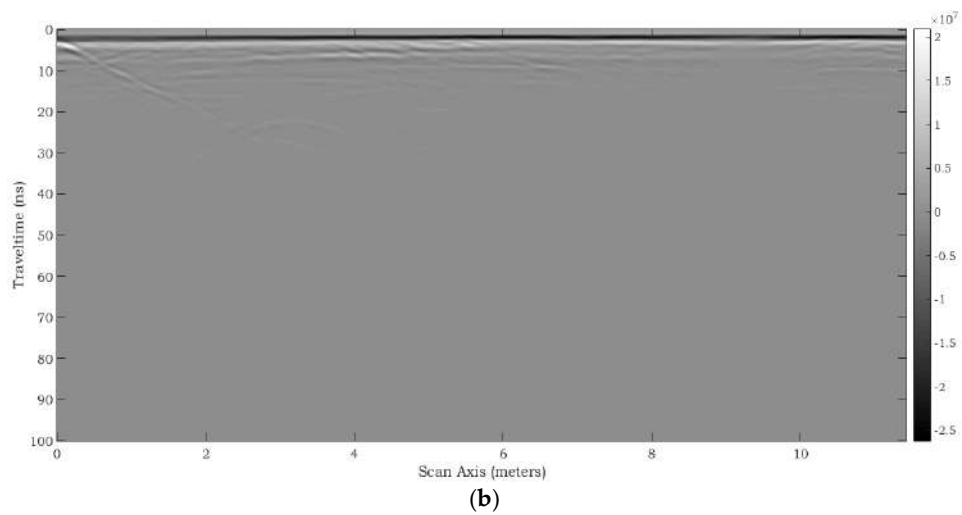


**Figure 36.** Profiles recorded in the Gneiss 0/20 gravel region by using GPR 1, on acquisition line 1, with last-generation antennas operating at: (a) 270 MHz; (b) 350 MHz.

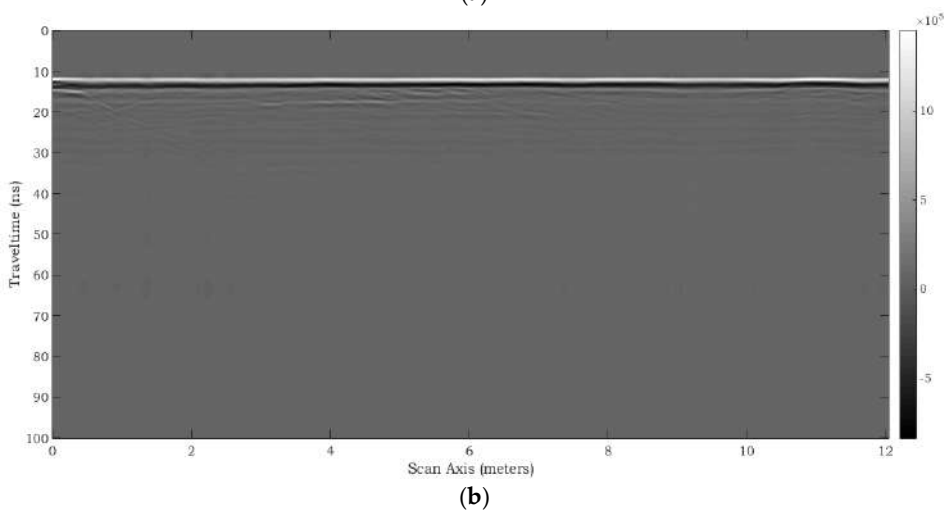
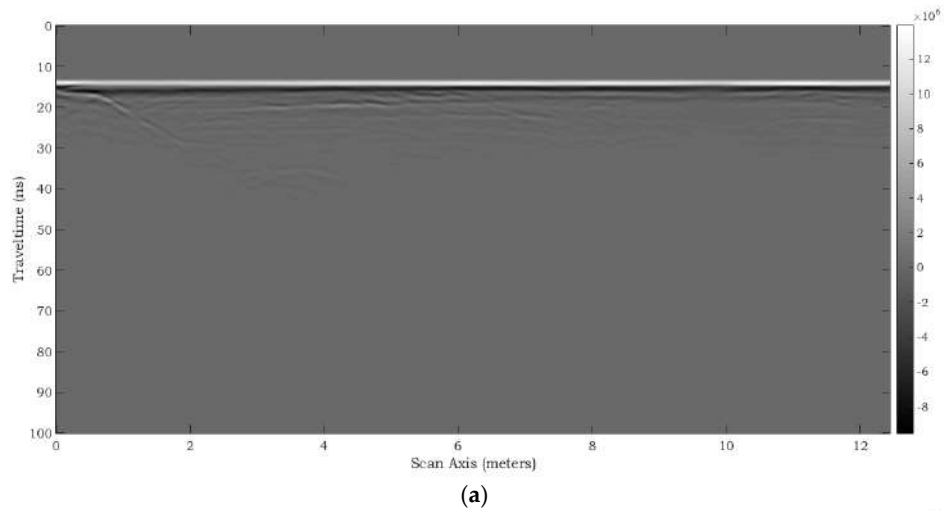


**Figure 37.** Profiles recorded in the Gneiss 0/20 gravel region by using GPR 1, on acquisition line 1, with last-generation antennas operating at: (a) 400 MHz; (b) 900 MHz.

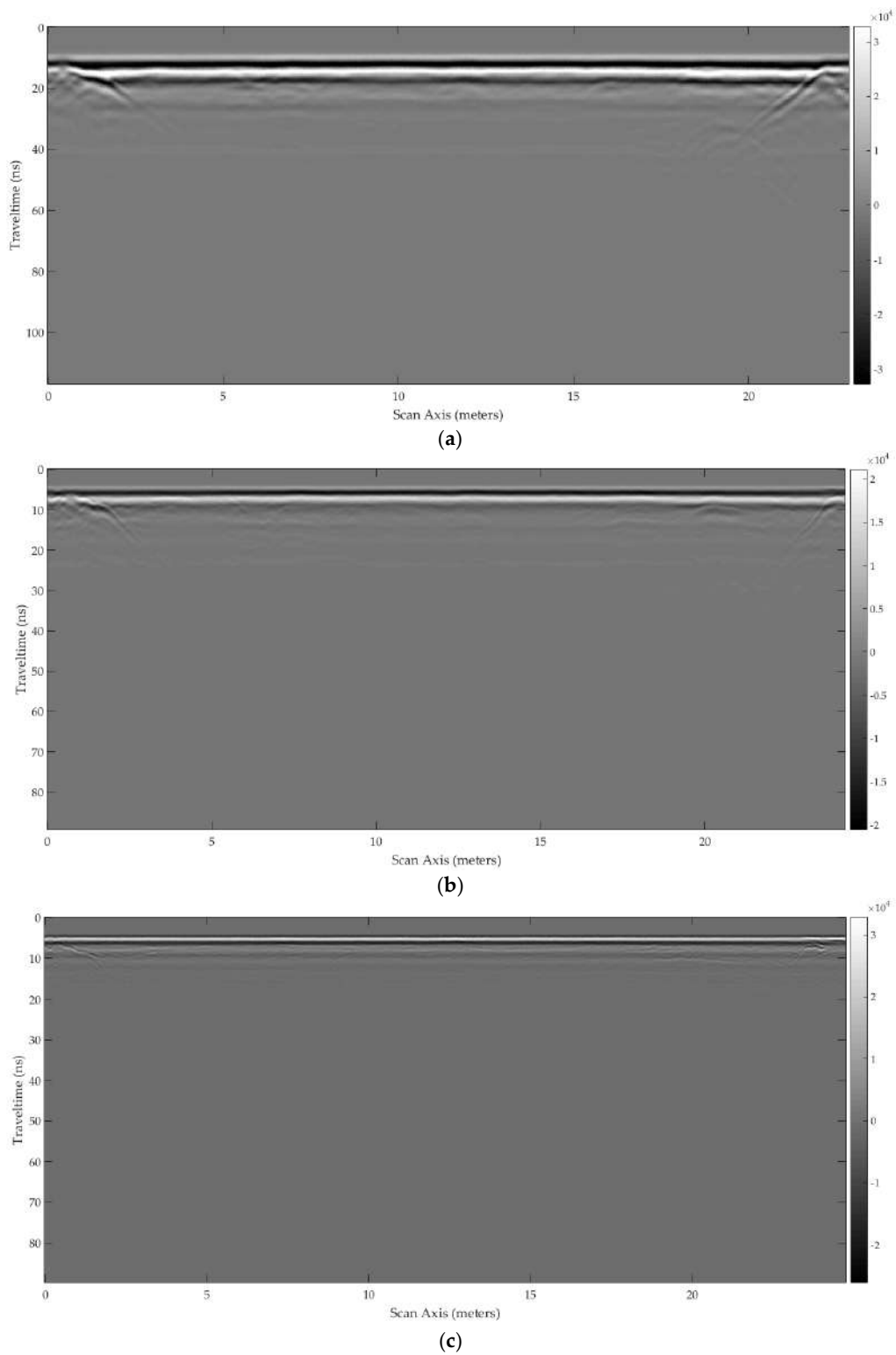


**Figure 38.** Profiles recorded in the Gneiss 0/20 gravel region by using GPR 2, on acquisition line 1, with antennas operating at: (a) 250 MHz; (b) 500 MHz; (c) 800 MHz.



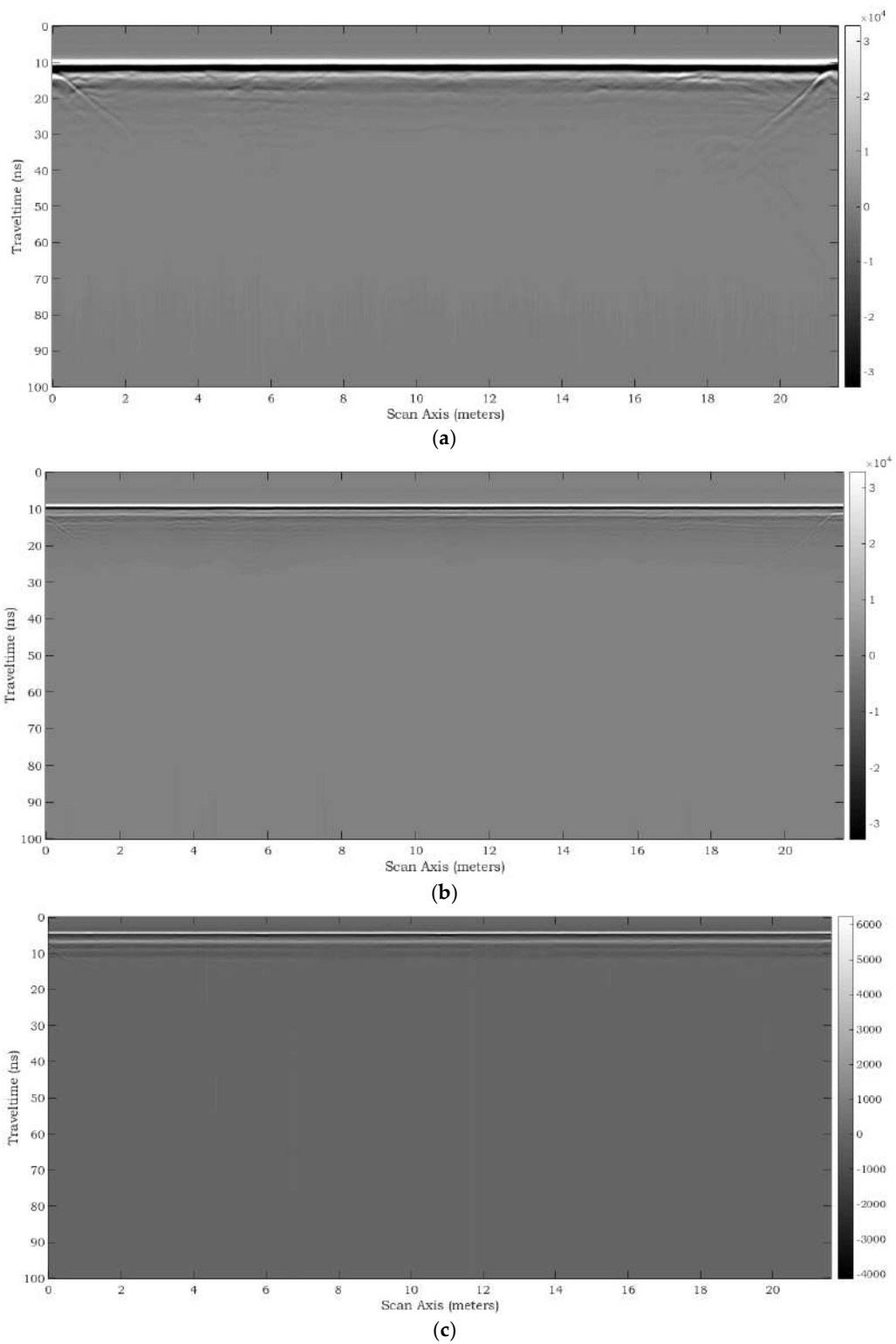
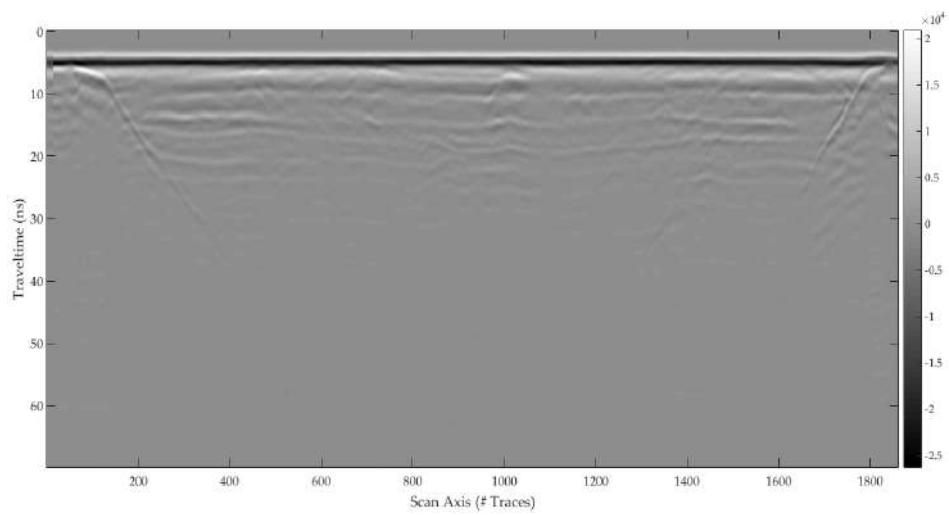
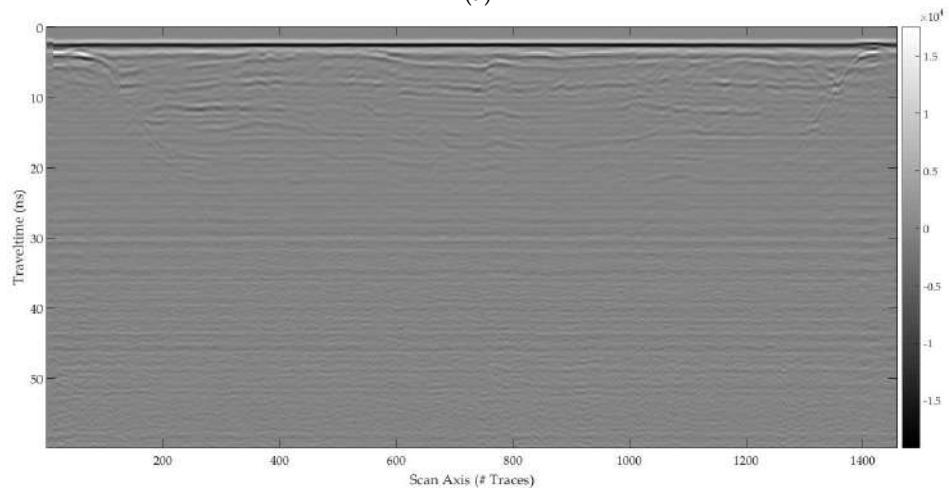


**Figure 39.** Profiles recorded in the Gneiss 0/20 gravel region by using GPR 3, on acquisition line 1, with antennas operating at: (a) 200 MHz; (b) 600 MHz; (c) 900 MHz.

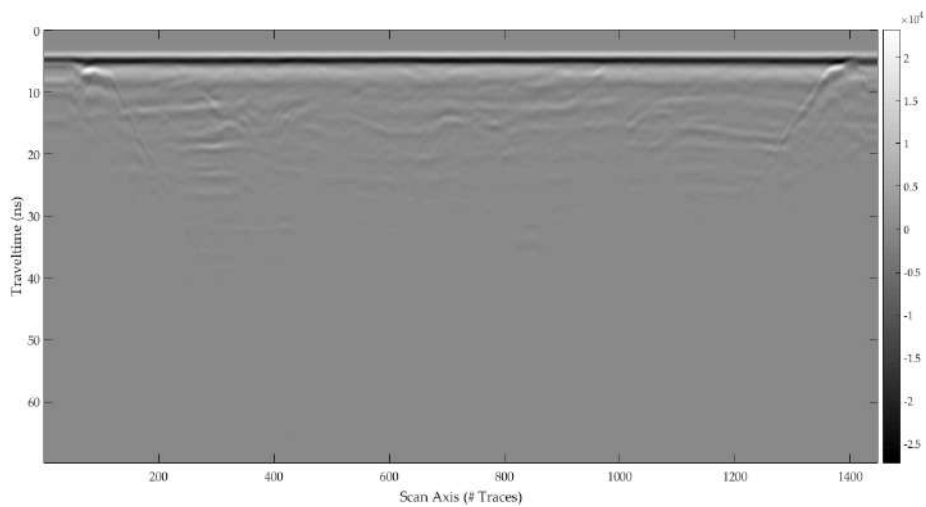


(a)



(b)

**Figure 40.** Profiles recorded in the Gneiss 0/20 gravel region by using GPR 1, on acquisition line 2, with antennas operating at: (a) 400 MHz; (b) 900 MHz.



(a)

**Figure 41.** Cont.

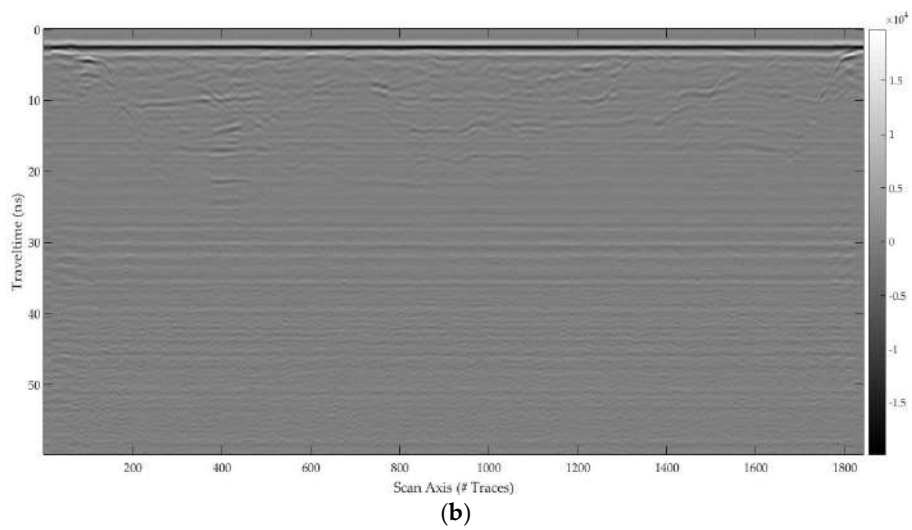


**Figure 41.** Profiles recorded in the Gneiss 0/20 gravel region by using GPR 1, on acquisition line 3, with antennas operating at: (a) 400 MHz; (b) 900 MHz.

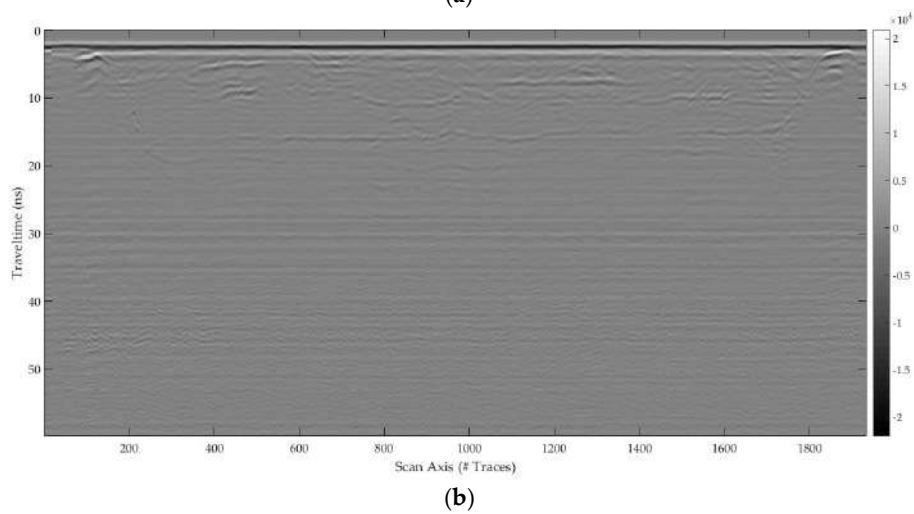
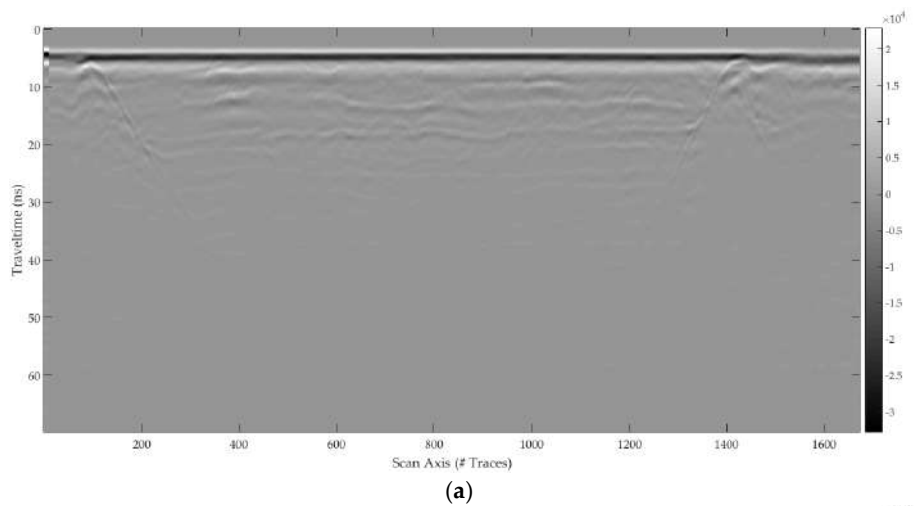


**Figure 42.** Profiles recorded in the Gneiss 0/20 gravel region by using GPR 1, on acquisition line 4, with antennas operating at: (a) 400 MHz; (b) 900 MHz.

## 6. Conclusions

The geophysical test site, built at the Nantes research center of the French institute of science and technology for transport, spatial planning, development and networks (IFSTTAR), was designed to test new geophysical techniques, innovative methods of measurement, and novel approaches for data analysis. It is proposed on a full-size scale and consists of a pit, 30 m long and 5 m wide at its maximum depth (around 4 m), with sloping sides that extend the width of the site to about 20 m. The pit is divided in five regions filled with different homogeneous soils and hosting georeferenced targets (such as pipes, artificial voids and rocks, masonry walls, etc.). The site was conceived to reserve margins of progress in the detection of heterogeneities by means of ground penetrating radar (GPR) or other geophysical techniques. Actually, some objects buried in the most conductive materials have not yet been detected from the surface.

In this paper, the geophysical test site and its construction process were described for the first time in detail. Then, a large dataset of GPR profiles, recorded by using three pulsed systems equipped with several antennas working in different frequency ranges, was presented. The profiles highlight the performances and limits of the GPR technique in terms of resolution and depth penetration versus soil and/or target. All results were accompanied by comments throughout the paper, and the effects of the application of pre-processing steps before saving the data were pointed out. All data files are found in an archive, enclosed to this paper as 'supplementary material'.

The presented dataset is the core part of the Open Database of Radargrams project of COST (European Cooperation in Science and Technology) Action TU1208 "Civil engineering applications of Ground Penetrating Radar". The idea beyond such initiative is to share with the scientific community a selection of GPR responses to enable an effective benchmark for direct and inverse electromagnetic scattering methods, imaging techniques and signal processing algorithms.

We hope that this dataset will be enriched by the contributions of further users, who are most welcome to visit the geophysical test site and collect new data with their GPR systems. We also hope that the dataset will be made alive by researchers who will process, analyze, invert and interpret the data, or implement electromagnetic models of the test site. It would be very interesting and useful to describe the state of the art of the research in the field by applying different techniques to the radargrams included in this dataset. At last, we hope that the challenge related to the multi-layer section will be achieved.

**Supplementary Materials:** The supplementary materials are available online at <https://zenodo.org/record/1211173#WsIuC1k0uUk>.

**Acknowledgments:** The authors are grateful to Mercedes Solla for inviting them to submit this paper to the Remote Sensing Special Issue "Recent Advances in GPR Imaging". They thank particularly J. L. Chazelas (Ifsttar) for the design and monitoring of the implementation of the geophysical test site, G. Gugole (Ifsttar) and F. Xie (The Hong Kong Polytechnic University) for performing some GPR measurements, and T. Dubreucq (Ifsttar) for the characterization of the materials. This work is a contribution to COST (European Cooperation in Science and Technology) Action TU1208 "Civil engineering applications of Ground Penetrating Radar" ([www.cost.eu](http://www.cost.eu), [www.GPRadar.eu](http://www.GPRadar.eu)). The authors thank COST for funding and supporting COST Action TU1208.

**Author Contributions:** The authors contributed equally to this work.

**Conflicts of Interest:** The authors declare no conflict of interest.

## References

1. Persico, R. *Introduction to Ground Penetrating Radar: Inverse Scattering and Data Processing*; Wiley-IEEE Press: Indianapolis, IN, USA, 2014; p. 392.
2. Benedetto, A.; Pajewski, L. (Eds.) *Civil Engineering Applications of Ground Penetrating Radar*. In *Springer Transactions in Civil and Environmental Engineering*; Springer International: New Delhi, India, 2015; p. 385. [[CrossRef](#)]

3. Chazelas, J.-L. *Création d'un Site-Test Pour les Méthodes Géophysiques Appliquées Aux Travaux Sans Tranchée—Rapport de Présentation Après Réalisation*; Technical Report No. 12; Laboratoire Central des Ponts et Chaussées: Nantes, France, 1998; p. 53. (In French)
4. Official Webpage of COST Action TU1208, Civil Engineering Applications of Ground Penetrating Radar on COST (European Cooperation in Science and Technology) Website. Available online: [http://www.cost.eu/COST\\_Actions/tud/TU1208](http://www.cost.eu/COST_Actions/tud/TU1208) (accessed on 28 March 2018).
5. Official Website of COST Action TU1208, Civil Engineering Applications of Ground Penetrating Radar. Available online: <http://www.GPRadar.eu> (accessed on 28 March 2018).
6. Eide, E.; Våland, P.A.; Sala, J. Ground-Coupled Antenna Array for Step-Frequency GPR. In Proceedings of the 15th International Conference on Ground Penetrating Radar (GPR 2014), Brussels, Belgium, 30 June–4 July 2014; pp. 756–761.
7. Huuskonen-Snicker, E.; Eskelinen, P.; Pellinen, T.; Olkkonen, M.-K. A New Microwave Asphalt Radar Rover for Thin Surface Civil Engineering Applications. *J. RF-Eng. Telecommun.* **2015**, *69*, 377–381. [[CrossRef](#)]
8. Ferrara, V.; Troiani, F.; Frezza, F.; Mangini, F.; Pajewski, L.; Simeoni, P.; Tedeschi, N. Design and Realization of a Cheap Ground Penetrating Radar Prototype@ 2.45 GHz. In Proceedings of the 2016 IEEE European Conference on Antennas and Propagation (EuCAP), Davos, Switzerland, 11–15 April 2016; pp. 1–4. [[CrossRef](#)]
9. Persico, R.; Leucci, G. Interference mitigation achieved with a reconfigurable stepped-frequency GPR system. *Remote Sens.* **2016**, *8*, 926. [[CrossRef](#)]
10. Ferrara, V.; Pietrelli, A.; Chicarella, S.; Pajewski, L. GPR/GPS/IMU system as buried objects locator. *Measurement* **2018**, *114*, 534–541. [[CrossRef](#)]
11. Fedeli, A.; Ježová, J.; Lambot, S. Testing of a new lightweight radar system for tomographical reconstruction of circular structures. In *Short-Term Scientific Missions: Years 4 & 5*; Pajewski, L., Rodriguez-Abad, I., Marciniak, M., Eds.; TU1208 GPR Association: Rome, Italy, 2018; pp. 18–44. Available online: <http://www.gpradar.eu/resources/books.html> (accessed on 28 March 2018).
12. Persico, R.; Provenzano, A.; Trela, C.; Sato, M.; Takahashi, K.; Arcone, S.; Koppenjan, S.; Stolarczyk, L.G.; Utsi, E.C.; Ebihara, S.; et al. *Recommendations for the Safety of People and Instruments in Ground-Penetrating Radar and Near-Surface Geophysical Prospecting*; EAGE: Houten, The Netherlands, 2015; p. 66.
13. Pajewski, L.; Persico, R.; Derobert, X.; Balayssac, J.-P.; Ebihara, S.; Grégoire, C.; Ivashchuk, V.; Kind, T.; Krysiński, L.; Wai-Lok Lai, W.; et al. *Catalogue of GPR Test Sites*; COST Action TU1208 Series; TU1208 GPR Association: Rome, Italy, 2017; Available online: <http://www.gpradar.eu/resources/books.html> (accessed on 28 March 2018). [[CrossRef](#)]
14. De Chiara, F.; Fontul, S.; Fortunato, E. GPR Laboratory Tests for Railways Materials Dielectric Properties Assessment. *Remote Sens.* **2014**, *6*, 9712–9728. [[CrossRef](#)]
15. Núñez-Nieto, X.; Solla, M.; Novo, A.; Lorenzo, H. Three-dimensional ground-penetrating radar methodologies for the characterization and volumetric reconstruction of underground tunneling. *Constr. Build. Mater.* **2014**, *71*, 551–560. [[CrossRef](#)]
16. Sagnard, F.; Norgeot, C.; Dérobert, X.; Baltazart, V.; Merliot, E.; Derkx, F.; Lebental, B. Utility detection and positioning on the urban site Sense-City using Ground-Penetrating Radar systems. *Measurement* **2016**, *88*, 318–330. [[CrossRef](#)]
17. Rodríguez-Abad, I.; Klysz, G.; Martínez-Sala, R.; Balayssac, J.-P.; Mené-Aparicio, J. Application of ground-penetrating radar technique to evaluate the waterfront location in hardened concrete. *Geosci. Instr. Methods Data Syst.* **2016**, *5*, 567–574. [[CrossRef](#)]
18. Dérobert, X.; Lataste, J.F.; Balayssac, J.-P.; Laurens, S. Evaluation of chloride contamination in concrete using electromagnetic non-destructive testing methods. *NDT E Int.* **2017**, *89*, 19–29. [[CrossRef](#)]
19. Reci, H.; Chinh Mai, T.; Mehdi Sbartai, Z.; Pajewski, L.; Kiri, E. Non-destructive evaluation of moisture content in wood by using Ground Penetrating Radar. *Geosci. Instr. Methods Data Syst.* **2016**, *5*, 575–581. [[CrossRef](#)]
20. Pajewski, L.; Fontul, S.; Solla, M. Ground Penetrating Radar for the evaluation and monitoring of transport infrastructures. In *Innovation in Near-Surface Geophysics: Instrumentation, Application and Data Processing Methods*; Persico, R., Piro, S., Linford, N., Eds.; Elsevier: Cambridge, MA, USA, 2018; in press.
21. Frezza, F.; Pajewski, L.; Ponti, C.; Schettini, G.; Tedeschi, N. Through-wall electromagnetic scattering by N conducting cylinders. *J. Opt. Soc. Am. A* **2013**, *30*, 1632–1639. [[CrossRef](#)] [[PubMed](#)]

22. Poljak, D.; Antonijević, S.; Šesnić, S.; Lalléchère, S.; Drissi, K.E.K. On deterministic-stochastic time domain study of dipole antenna for GPR applications. *Eng. Anal. Bound. Elem.* **2016**, *73*, 14–20. [[CrossRef](#)]
23. Warren, C.; Sesnic, S.; Ventura, A.; Pajewski, L.; Poljak, D.; Giannopoulos, A. Comparison of Time-Domain Finite-Difference, Finite-Integration, and Integral-Equation Methods for Dipole Radiation in Half-space Environments. *Prog. Electromagn. Res. M (PIER M)* **2017**, *57*, 175–183. [[CrossRef](#)]
24. Prokopovich, I.; Popov, A.; Pajewski, L.; Marciniak, M. Application of coupled-wave Wentzel-Kramers-Brillouin approximation to Ground Penetrating Radar. *Remote Sens.* **2018**, *10*, 22. [[CrossRef](#)]
25. André, F.; Lambot, S. Intrinsic Modeling of Near-Field Electromagnetic Induction Antennas for Layered Medium Characterization. *IEEE Trans. Geosci. Remote Sens.* **2014**, *52*, 7457–7469. [[CrossRef](#)]
26. De Coster, A.; Tran, A.P.; Lambot, S. Fundamental Analyses on Layered Media Reconstruction Using GPR and Full-Wave Inversion in Near-Field Conditions. *IEEE Trans. Geosci. Remote Sens.* **2016**, *54*, 5143–5158. [[CrossRef](#)]
27. Ristic, A.; Bugarinovic, Z.; Vrtunski, M.; Govedarica, M. Point Coordinates Extraction from Localized Hyperbolic Reflections in GPR Data. *J. Appl. Geophys.* **2017**, *144*, 1–17. [[CrossRef](#)]
28. Nounouh, S.; Eyraud, C.; Litman, A.; Tortel, H. Near-subsurface imaging in an absorbing embedding medium with a multistatic/single frequency scanner. *Near Surf. Geophys.* **2015**, *13*, 211–218. [[CrossRef](#)]
29. Mertens, L.; Persico, R.; Matera, L.; Lambot, S. Automated Detection of Reflection Hyperbolas in Complex GPR Images With No A Priori Knowledge on the Medium. *IEEE Trans. Geosci. Remote Sens.* **2016**, *54*, 580–596. [[CrossRef](#)]
30. Salucci, M.; Poli, L.; Anselmi, N.; Massa, A. Multifrequency Particle Swarm Optimization for Enhanced Multiresolution GPR Microwave Imaging. *IEEE Trans. Geosci. Remote Sens.* **2017**, *55*, 1305–1317. [[CrossRef](#)]
31. Varela-González, M.; Solla, M.; Martínez-Sánchez, J.; Arias, P. A semi-automatic processing and visualisation tool for ground-penetrating radar pavement thickness data. *Autom. Constr.* **2014**, *45*, 42–49. [[CrossRef](#)]
32. Li, J.; Le Bastard, C.; Wang, Y.; Wei, G.; Ma, B.; Sun, M. Enhanced GPR Signal for Layered Media Time-Delay Estimation in Low-SNR Scenario. *IEEE Geosci. Remote Sens. Lett.* **2016**, *13*, 299–303. [[CrossRef](#)]
33. Economou, N. Time-varying band-pass filtering GPR data by self-inverse filtering. *Near Surf. Geophys.* **2016**, *14*, 207–217. [[CrossRef](#)]
34. Warren, C.; Giannopoulos, A.; Giannakis, I. GPRMax: Open source software to simulate electromagnetic wave propagation for Ground Penetrating Radar. *Comput. Phys. Commun.* **2016**, *209*, 163–170. [[CrossRef](#)]
35. Pirrone, D.; Pajewski, L. E<sup>2</sup>GPR—Edit your geometry, Execute GprMax2D and Plot the Results. In Proceedings of the 2015 IEEE 15th Mediterranean Microwave Symposium, Lecce, Italy, 30 November–2 December 2015; pp. 1–4. [[CrossRef](#)]
36. Pajewski, L.; Giannopoulos, A.; Pirrone, D.; Warren, C.; Antonijevic, S.; Doric, V.; Poljak, D. Development of electromagnetic simulators for Ground Penetrating Radar. In Proceedings of the 2017 Conference of the Applied Computational Electromagnetics Society, Florence, Italy, 26–30 March 2017; pp. 1–2. [[CrossRef](#)]
37. Meschino, S.; Pajewski, L. SPOT-GPR: A freeware tool for target detection and localization in GPR data developed within the COST Action TU1208. *J. Telecommun. Inf. Technol.* **2017**, *2017*, 43–54. [[CrossRef](#)]
38. Meschino, S.; Pajewski, L. A practical guide on using SPOT-GPR, a freeware tool implementing a SAP-DoA technique. *Ground Penetr. Radar* **2018**, *1*, 104–122. [[CrossRef](#)]
39. Riveiro, B.; Solla, M. *Non-Destructive Techniques for the Evaluation of Structures and Infrastructure*. Structures and Infrastructures; CRC Press: Boca Raton, FL, USA, 2016; p. 398.
40. Santos-Assunção, S.; Perez-Gracia, V.; Caselles, O.; Clapes, J.; Salinas, V. Assessment of Complex Masonry Structures with GPR Compared to Other Non-Destructive Testing Studies. *Remote Sens.* **2014**, *6*, 8220–8237. [[CrossRef](#)]
41. Persico, R.; D’Amico, S. Use of Ground Penetrating Radar and standard geophysical methods to explore the subsurface. *Ground Penetr. Radar* **2018**, *1*, 1–37. [[CrossRef](#)]
42. Solla, M.; Fontul, S. Non-destructive tests for railway evaluation: Detection of fouling and joint interpretation of GPR data and track geometric parameters. *Ground Penetr. Radar* **2018**, *1*, 75–103. [[CrossRef](#)]
43. Solla, M.; Lagüela, S. Thermography: Principles and applications. *Ground Penetr. Radar* **2018**, *1*, 123–141. [[CrossRef](#)]
44. Núñez-Nieto, X.; Solla, M.; Gómez-Pérez, P.; Lorenzo, H. GPR Signal Characterization for Automated Landmine and UXO Detection Based on Machine Learning Techniques. *Remote Sens.* **2014**, *6*, 9729–9748. [[CrossRef](#)]



45. Santos-Assunção, S.; Perez-Gracia, V.; Salinas, V.; Caselles, O.; Gonzalez-Drigo, R.; Pujades, L.G.; Lantada, N. GPR Backscattering Intensity Analysis Applied to Detect Paleochannels and Infilled Streams for Seismic Nanozonation in Urban Environments. *IEEE J. Sel. Top. Appl. Earth Obs. Remote Sens.* **2016**, *9*, 167–177. [[CrossRef](#)]
46. Jezova, J.; Mertens, L.; Lambot, S. Ground-penetrating radar for observing tree trunks and other cylindrical objects. *Constr. Build. Mater.* **2016**, *123*, 214–225. [[CrossRef](#)]
47. Ceru, T.; Segina, E.; Gosar, A. Geomorphological Dating of Pleistocene Conglomerates in Central Slovenia Based on Spatial Analyses of Dolines Using LiDAR and Ground Penetrating Radar. *Remote Sens.* **2018**, *9*, 1213. [[CrossRef](#)]
48. Pérez-Gracia, V.; Caselles, J.-O.; Clapés, J.; Martínez, G.; Osorio, R. Non-destructive analysis in cultural heritage buildings: Evaluating the Mallorca cathedral supporting structures. *Non Destr. Test. Eval. Int.* **2013**, *59*, 40–47. [[CrossRef](#)]
49. Santos-Assunção, S.; Dimitriadis, K.; Konstantakis, Y.; Perez-Gracia, V.; Anagnostopoulou, E.; Gonzalez-Drigo, R. Ground-penetrating radar evaluation of the ancient Mycenaean monument Tholos Acharnon tomb. *Near Surf. Geophys.* **2016**, *14*, 197–205. [[CrossRef](#)]
50. Solla, M.; Asorey-Cacheda, R.; Núñez-Nieto, X.; Conde-Carnero, B. Evaluation of historical bridges through recreation of GPR models with the FDTD algorithm. *Constr. Build. Mater.* **2016**, *77*, 19–27. [[CrossRef](#)]
51. Pajewski, L.; Solla, M.; Küçükdemirci, M. Ground-Penetrating Radar for Archaeology and Cultural-Heritage Diagnostics: Activities Carried Out in COST Action TU1208. In *Nondestructive Techniques for the Assessment and Preservation of Historic Structures*; Goncalves, L., Rodrigues, H., Gaspar, F., Eds.; Book Chapter No. 13; CRC Press: Boca Raton, FL, USA, 2017; pp. 215–225.
52. Persico, R.; D’Amico, S.; Rizzo, E.; Capozzoli, L.; Micallef, A. Ground Penetrating Radar investigations in sites of cultural interest in Malta. *Ground Penetr. Radar* **2018**, *1*, 38–61. [[CrossRef](#)]
53. Pajewski, L.; Giannopoulos, A. Electromagnetic modelling of Ground Penetrating Radar responses to complex targets. In *Short Term Scientific Missions and Training Schools—Year 1, COST Action TU1208*; Pajewski, L., Marciniak, M., Eds.; Aracne Editrice: Rome, Italy, 2014; pp. 7–45. Available online: <http://www.gpradar.eu/resources/books.html> (accessed on 28 March 2018).
54. COST Action TU1208. *Proceedings of the 2015 WG Progress Meeting, Edinburgh, UK, April 2015*; Pajewski, L., Ed.; Aracne Editrice: Rome, Italy, 2015.
55. Pajewski, L.; Giannopoulos, A.; van der Kruk, J. Electromagnetic modelling, inversion and data-processing techniques for GPR: Ongoing activities in Working Group 3 of COST Action TU1208. In *Proceedings of the 2015 European Geosciences Union (EGU) General Assembly, Vienna, Austria, 12–17 April 2015*; abstract ID EGU2015-14988.
56. McGahan, R.V.; Kleinman, R.E. Second annual special session on image reconstruction using real data. *IEEE Antennas Propag. Mag.* **1997**, *39*, 7–32. [[CrossRef](#)]
57. McGahan, R.V.; Kleinman, R.E. Third annual special session on image reconstruction using real data: Part 1. *IEEE Antennas Propag. Mag.* **1999**, *41*, 34–51. [[CrossRef](#)]
58. McGahan, R.V.; Kleinman, R.E. Third annual special session on image reconstruction using real data: Part 2. *IEEE Antennas Propag. Mag.* **1999**, *41*, 20–40. [[CrossRef](#)]
59. Belkebir, K.; Saillard, M. Special section: Testing inversion algorithms against experimental data. *Inverse Probl.* **2001**, *17*, 1565–1571. [[CrossRef](#)]
60. Belkebir, K.; Saillard, M. Special section: Testing inversion algorithms against experimental data: Inhomogeneous targets. *Inverse Probl.* **2005**, *21*, S1–S3. [[CrossRef](#)]
61. Geffrin, J.-M.; Sabouroux, P.; Eyraud, C. Free space experimental scattering database continuation: Experimental set-up and measurement precision. *Inverse Probl.* **2005**, *21*, S117–S130. [[CrossRef](#)]
62. Geffrin, J.-M.; Sabouroux, P. Continuing with the Fresnel database: Experimental setup and improvements in 3D scattering measurements. *Inverse Probl.* **2009**, *25*, 024001. [[CrossRef](#)]
63. Versteeg, R. The Marmousi experience: Velocity model determination on a synthetic complex data set. *Lead. Edge* **1994**, *13*, 927–936. [[CrossRef](#)]
64. Musumeci, C.; Cocina, O.; De Gori, P.; Patanè, D. Seismological evidence of stress induced by dike injection during the 2001 Mt. Etna eruption. *Geophys. Res. Lett.* **2004**, *31*, L07617. [[CrossRef](#)]
65. Solla, M.; Lorenzo, H.; Riveiro, B. Non-destructive methodologies in the assessment of the masonry arch bridge of Traba, Spain. *Eng. Fail. Anal.* **2011**, *18*, 828–835. [[CrossRef](#)]

66. Warren, C.; Giannopoulos, A. *gprMax/iwagpr2017-model: v.1.0*; Version v.1.0; Zenodo: Geneva, Switzerland, 2017. [[CrossRef](#)]
67. Grandjean, G.; Gourry, J.C.; Bitri, A. Evaluation of GPR techniques for civil-engineering applications: Study on a test site. *J. Appl. Geophys.* **2000**, *45*, 141–156. [[CrossRef](#)]
68. Ferber, V. *Déformations Induites Par L'humidification de Sols Fins Compactés, Apport d'un Modèle de Microstructure*; GT80; Laboratoire Central des Ponts et Chaussées (LCPC): Bouguenais, France, 2006; 321p, ISBN 2-7208-2464-X.
69. Skempton, A.W. A study of the geotechnical properties of some post-glacial clays. *Géotechnique* **1948**, *1*, 111–124. [[CrossRef](#)]
70. Tzanis, A. *MATGPR: A Brief Introduction*. In *Proceedings of the 2014 Working Group Progress Meeting, Nantes, FR, February 2014*; Pajewski, L., Derobert, X., Eds.; COST Action TU1208 Series; Aracne Editrice: Rome, Italy, 2014; pp. 39–68. Available online: <http://www.gpradar.eu/resources/books.html> (accessed on 28 March 2018).



© 2018 by the authors. Licensee MDPI, Basel, Switzerland. This article is an open access article distributed under the terms and conditions of the Creative Commons Attribution (CC BY) license (<http://creativecommons.org/licenses/by/4.0/>).